UC Davis

UC Davis Previously Published Works

Title

High-Fidelity Numerical Simulations of Side-by-Side Rotor with Ground Effect

Permalink

https://escholarship.org/uc/item/2nw9485v

Journal

Journal of the American Helicopter Society, 70(3)

ISSN

0002-8711

Authors

Sagaga, Jared

Lee, Seongkyu

Publication Date

2025

DOI

10.4050/jahs.70.032004

Peer reviewed

eScholarship.org Powered by the California Digital Library
University of California

High-Fidelity Numerical Simulations of Side-by-Side Rotor with Ground Effect

Jared Sagaga

Aerospace Engineer

CFD Research Corporation

Huntsville, AL

Seongkyu Lee

Professor

Department of Mechanical and Aerospace Engineering

University of California

Davis, CA

Abstract

This study examines the effects of ground proximity on the performance, aerodynamics, and aeroacoustics of NASA's side-by-side urban air mobility reference vehicle rotors in hover, utilizing high-fidelity computational fluid dynamics and aeroacoustic simulations. Two rotor overlap configurations (0% and 25%) at two different heights above the ground plane are evaluated. Results indicate that the ground plane significantly influences rotor performance, with the figure of merit improving as the rotor-ground distance decreases. The 0% overlap configuration shows increased blade sectional thrust, pressure fluctuations, and noise levels compared to the 25% overlap configuration, primarily due to reduced induced velocity; without rotor overlap, upwash flow more easily reaches the rotor disk plane. Aerodynamic interactions intensify with proximity to the ground, particularly as rotor-ground distance decreases. Notably, the 25% overlap configuration provides a noise reduction of 3–4 dBA near the ground compared to the 0% overlap setup. However, despite its noise reduction benefit, the 25% overlap configuration poses greater safety concerns close to the ground, as indicated by

an elevated hazardousness factor relative to the 0% overlap configuration. Finally, noise directivity exhibits substantial differences between A-weighted and unweighted overall sound pressure levels, with A-weighting mitigating acoustic interference effects.

Nomenclature

A Rotor disk area, m^2

A_{proj} Projected area, m^2

C_nM^2 Non-dimensional sectional normal force

d Hub separation distance, m

D Rotor diameter, m

C_T Thrust coefficient, $\frac{T}{\rho A R^2 \Omega^2}$

C_Q Torque coefficient, $\frac{Q}{\rho A R^3 \Omega^2}$

FM Figure of merit, $\frac{T_{total}}{P_{total}} \sqrt{\frac{T_{total}}{2\rho A_{proj}}}$

F_z Sectional normal force, N/m

M_r $\vec{M} \cdot \hat{r}$

T Thrust, N

Q Torque, $N \cdot m$

P_{Total} Total power, W

r Observer radial distance, m

R Rotor radius, m

T_{Total} Total thrust, N

t Observer time, s

y^+ Dimensionless wall distance

Greek Symbols

λ_i Induced inflow ratio

Ω Rotor rotation rate, $\frac{rad}{s}$

Ψ Azimuth angle, deg

ρ_∞ Air density, $\frac{kg}{m^3}$

Acronyms

BVI Blade-vortex interaction

CFD Computational fluid dynamics

CCW Counterclockwise

CW Clockwise

DVE Degraded visual environment

IGE In-ground effect

LTC Lieutenant Colonel

OASPL Overall sound pressure level

OGE Out-of-ground effect

SbS Side-by-Side

SPL Sound pressure level

UAM Urban Air Mobility

VTOL Vertical take-off and landing

Introduction

The burgeoning Urban Air Mobility (UAM) market, featuring fully electric or hybrid-electric Vertical Take-Off and Landing (VTOL) aircraft, has garnered significant interest as a solution to increasing urban congestion. Operating in densely populated cities experiencing strained transportation networks, UAM faces challenges in safety, traffic management, autonomy, and noise, the latter being a crucial barrier to its success. For example, Uber [1] suggested that UAM noise should be 15 dBA lower than a similar-sized helicopter's noise. Rimjha et al. [2] corroborated Uber's claim, finding that a 15 dBA noise reduction leads to an 80% reduction in the land area impacted by noise and the overall highly annoyed population. However, Jia and Lee [3, 4] and Li and Lee [5] found that achieving a noise level 15 dBA lower than helicopter noise is challenging. In addition, they addressed that UAM aircraft could generate higher noise than background noise from highways or residential communities at or below 1000 ft altitude.

Recent research has employed computational and experimental methods to develop a comprehensive understanding of UAM aircraft acoustics [6, 7, 8], focusing on key noise sources, noise directivity,

broadband noise, and aerodynamic interactions in small, fixed-pitch, variable RPM rotor configurations [4, 3, 5, 9, 10, 11]. Acoustics also plays a crucial role in UAM aircraft design [12, 13] and trajectory optimization [6, 7, 8], typically employing low-fidelity acoustic prediction tools for implementation [14]. However, most UAM noise studies did not consider the ground effect on aerodynamics and acoustics. As the UAM field expands and produces diverse multi-rotor designs, significant interactional aerodynamics will occur when operating near ground surfaces. A few recent investigations have highlighted the importance of in-ground-effect (IGE) on performance, aerodynamics, control, and acoustics for single rotor [15], dual rotors [16, 17, 18] and quadcopter [19].

Ground effect affects rotorcraft performance due to the presence of a boundary (e.g. ground) inhibiting rotor wake development. However, the aerodynamics and acoustics of multi-rotor vehicles in these conditions are not yet fully understood. Previous experimental studies reported improvements in rotor thrust and power when a ground plane was present at distances of one or two rotor radii. When a rotorcraft hovers near the ground surface (e.g., at rotor heights of one or two rotor radii), the rotor wake initially propagates downward before rapidly expanding upon approaching the ground. This expansion changes the flow from vertical downwash to radial outwash, developing a radial wall jet that alters induced and slipstream velocities, affecting thrust and power [20]. Although numerous past studies have investigated ground surface effects, most focused on isolated rotors or single main rotor full vehicle configurations.

Rotorwash or downwash, the powerful downdraft generated by a helicopter or other rotorcraft's rotating blades, can pose a significant hazard, especially in UAM operations. This paper explores the effects of rotorwash, particularly the danger from the outwash generated by the wake of rotors, which may exert high pressure on ground personnel and equipment. The risk extends to potentially causing loose ground objects like debris to become airborne hazards. Existing research such as Ferguson's FAA report (FAA TR FAAJRD-93/31) [21] and Preston et al.'s study [22] delve into environmental limits and rotorwash modeling for military and civil operations. Rovere et al. [23] and Jung et al. [24] provide insights into rotor safety and aerodynamic performance in-ground effect, while George et al. [25] and Stephenson [26] emphasize the increased danger from high disk loading aircraft. However, a research gap exists concerning multi-rotor UAM aircraft in proximity to the ground, emphasizing the need for further investigation in this area.

The NASA Side-by-Side (SbS) aircraft as shown in Fig. 1, a focus of extensive research [27, 28, 4, 29, 30, 18], features two overlapping, intermeshing main rotors. This design provides a compact structure well-suited for UAM operations. Notably, the SbS configuration is expected to achieve a significant reduction in emissions and power consumption compared to conventional single main rotor helicopters. It also stands out as the lightest among NASA's UAM reference vehicles [31, 32]. Furthermore, the SbS rotor, characterized by its low disk loading, demonstrates enhanced cruise efficiency, especially when compared to tilt-rotor configurations [33].

Fig. 1: Six-passenger side-by-side air taxi VTOL concept design rendering from NASA [34].

The goal of this paper is to investigate the impact of the ground plane on the performance, aerodynamics (including rotor-to-rotor interactions), and aerodynamically induced noise of the SbS rotor (without the fuselage) in hover using high-fidelity computational fluid dynamics (CFD). Analysis of the average velocity and amplitude of the fluctuations in a plane parallel to the ground plane are quantified for all cases considered. The presence of the ground plane also causes significant variations in acoustic intensity and directivity at two heights above the ground and with distinct rotor overlap settings. We note that this paper solely focuses on the tonal noise generated from rotor blades. Li and Lee [5, 9, 35, 36] highlighted the importance of broadband noise in rotorcraft noise including SbS rotor. However, broadband noise will not be considered in the current paper.

Methodology

The first-principles unsteady and compressible Navier-Stokes equations are solved to capture unsteady aerodynamics, radial flow, swirl, compressibility, flow separation, and blade-vortex interaction for the rotating blades. CFD calculations are performed using CREATE^{TM}-AV Helios [37], with the OVERFLOW

module for near-body calculations and SAMCart for off-body calculations. The off-body meshes use structured meshing with adaptive mesh refinement (AMR) to help resolve tip vortices. Simulations in the present work only include the left (CW) and right (CCW) rotors, excluding the fuselage. A 45° phase shift is applied to the left rotor, as seen in Fig. 2. To investigate the effect of overlap distance between the left and right rotors, different overlapping cases, including 0% and 25% with a collective pitch angle of 8°, are considered. The overlap region percentage is determined by the distance between the two rotors. These overlap distances are nondimensionalized using the rotor radius (R). The separation distances between the left and right rotor centers for 0% and 25% overlap correspond to $2R$ and $1.5R$, respectively. As the material properties are unavailable from the vehicle's initial design phase, the rotor blades are modeled as rigid (no elastic deformation). Other vehicle design parameters are presented in Table 1. Details on the CFD solver, grids, and settings are outlined in subsequent sections. The Boeing VR-12 and Sikorsky SSC-A09, two modern airfoils, are used for the rotor blades. Along the span, the VR-12 is used at $R < 85\%$, and the SSC-A09 is used at $R > 95\%$. Linear interpolation between the SSC-A09 and VR-12 is assumed for the 85% and 95% spanwise locations. The blade chord is constant until 94% blade radius and twist distribution is assumed linear with a linear twist of -4°. Between the rotor radius of 94% and the blade tip, a 15° linear swept-tapered ratio is applied, as shown in Fig. 3, which depicts the blade planform.

Table 1: Basic properties for the side-by-side air taxi

Rotors	2
Blades per Rotor	4
Rotor Radius	10.5 ft (3.2 m)
Tip Chord Length	0.43 ft (0.13 m)
Chord Length	0.711 ft (0.217 m)
Nominal Rotor Speed	499.97 RPM
Nominal Rotor Tip Speed	621.7 ft/s (189.5 m/s)
Gross Weight	3,950 lb (1,792 kg)

CFD Simulation Setup

OVERFLOW [38], a high-fidelity and overset structured flow solver developed and maintained by NASA, is employed as the near-body solver in Helios. OVERFLOW has been extensively used in the field of multi-rotor aerodynamics and aeroacoustics. For instance, Jia and Lee and Sagaga and Lee applied

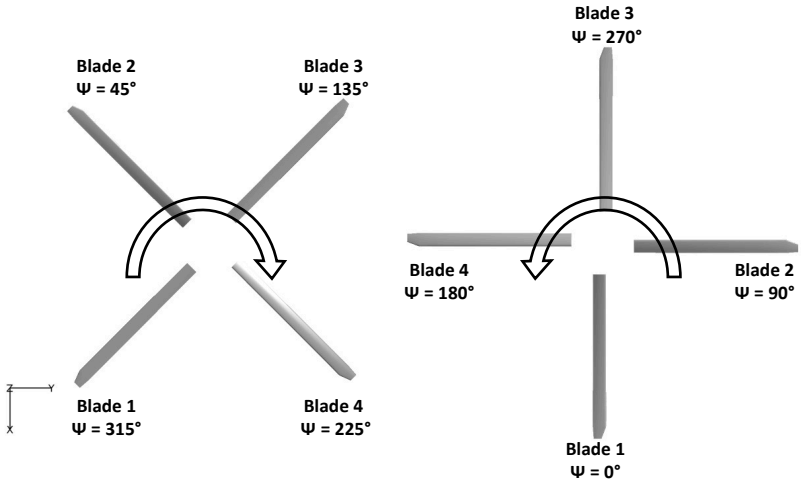

Fig. 2: Side-by-side rotor configuration with no overlap.

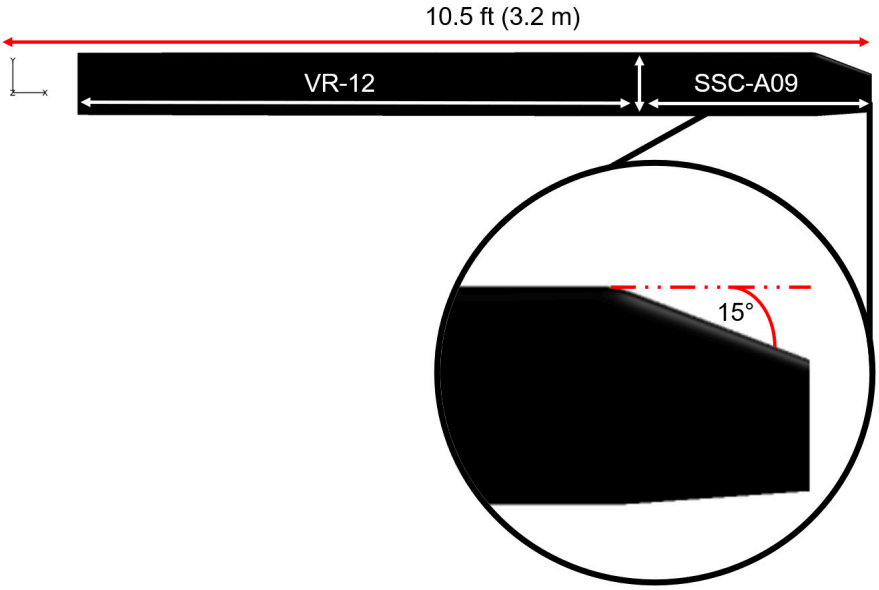

Fig. 3: Rotor blade planform.

OVERFLOW to study the aeroacoustics of coaxial rotors [39, 40, 41], quadrotors [3], and side-by-side rotors [4, 29, 30] employing similar best practices outlined in a study by Chaderjian for accurate CFD simulation of rotorcraft [42]. An off-body Cartesian solver, SAMCart, in conjunction with AMR, captures the rotor wakes and tip vortices shedding. In OVERFLOW, a fifth-order central difference spatial scheme is applied for the inviscid terms. For the viscous terms, a second-order discretization scheme is utilized. Temporal discretization employs a second-order diagonalized Beam Warming pentadiagonal scheme, along with dual-time stepping subiterations. The Spalart-Allmaras detached eddy simulation (DES) option is used to resolve viscous turbulent flows outside the boundary layer on the wall and the

wakes in the off-body. A rotation curvature correction model is employed. Time-accurate simulations for the present work are divided into two different time-step simulations to reduce computational time. The time-step size varies from 10° to 2.0° azimuth in increments of 2° for 3,288 timesteps or the first 40 rotor revolutions. A restart is then initiated in the subsequent runs, switching to a finer time-step after 40 rotor revolutions, where the finest time-step size of 0.25° azimuth is used for the final 5 rotor revolutions or 7,200 timesteps. The number of sub-iterations in the off-body is set to 10. In the near-body, it varies from 80 to 20 with an increment of 20 changing from a time-step size of 10° to 0.25°. All CFD simulations were conducted on the Onyx (Cray XC40/50) high-performance computer (HPC) maintained by the U.S. Army Engineer Research and Development Center, one of the U.S. Department of Defense (DoD) Supercomputing Resource Centers (DSRC). A total of 21 nodes (924 cores) were utilized for all simulations. Tables 2 and 3 display the simulation settings and present the breakdown of the computational grid size and cost for each IGE simulation, respectively.

Table 2: Simulation settings | All overlap cases

Near-body settings	
Grid type	Structured grid
Spatial scheme	Fifth-order accurate
Turbulence model	SA-DES with rotation correction
Off-body settings	
Grid type	Cartesian AMR
Finest wake-grid spacing	10% C_{tip} spacing
Spatial scheme	Fifth-order accurate
Turbulence model	SA-DES

CFD Grids

An overset mesh paradigm is employed in Helios, as mentioned earlier, which divides the entire computational domain into the near-body and off-body mesh systems. The rotor blades are modeled using an overset structured mesh for the near-body with an O-grid topology, and the far-field is modeled in the off-body using an adaptive Cartesian grid. The near-body mesh is created with NASA's Chimera Grid Tools (CGT), an overset grid generation software [43]. Figure 4 shows the surface mesh of the blade at

Table 3: Computational size and cost | All overlap cases

Near-body grid	
Per rotor blade	4.9 million
Both rotors	39.2 million
Off-body grid	
AMR OFF	170 million
AMR ON	705 million (H/D = 1)
	520 million (H/D = 0.5)
Number of processors	924
Simulation time per rotor revolution (hrs)	28 | First 40 revs
	72 | Last 5 revs

the blade root and tip. As for the details on grid resolution, there are 265 points around the airfoil, 165 points in the spanwise direction, and 65 points in the normal direction. The spacings at the leading and trailing edges are set to be 0.05% C_{tip} and 0.02% C_{tip}, respectively, with C_{tip} being the tip chord of the blade. The spacing at the wall of 1.0×10^{-5} meters is used to achieve a y^+ (dimensionless wall distance) of 1.0.

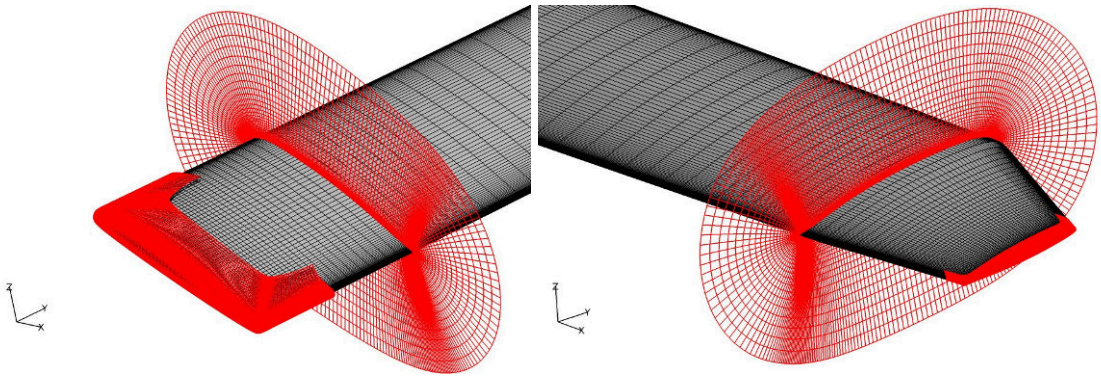

(a) (b)

Fig. 4: Near-body grids of the rotor blade: (a) blade root and (b) blade tip.

In the near-body volume grids, the end spacing is set to be 10% C_{tip}. For the off-body Cartesian volume grids, the finest spacing is also set to be 10% of the C_{tip}. The number of points for each rotor blade is approximately 4.9 million, and a total of 39.2 million grid points are used for all eight rotor blades, as shown in Table 3.

The Cartesian grid in the off-body is automatically generated by SAMCart using eight refinement levels

with AMR activated after 40 rotor revolutions (3,288 timesteps). AMR is a capability in SAMCart, which helps capture the detailed physics of the rotor wakes, including all shedding tip vortices within the defined AMR region, as seen in Fig. 5. There is a fixed refinement box surrounding the two rotors, used to resolve and capture the flow physics and wake near the rotor blades. The spacing in the fixed refinement box is set to be 10% C_{tip}, matching the spacing on the outer boundary of the near-body volume grids, and its spacing does not change throughout the simulation duration, unlike the AMR region. Setting a fixed refinement box enveloping both rotors with an adaptive region set below the fixed refinement box for tracking the shedding vortices, especially in the far-wake, can also help reduce the cost for these types of simulation cases. The size of the refinement box is set to $1.25R$ in the x-direction, $2.5R$ in the y-direction, $0.25R$ in the z-direction as shown in Fig. 5. The AMR region has similar sizing to the refinement in the x and y directions; however, it is set to be $1R$ and $2R$ for $H/D = 0.5$ and $H/D = 1$ cases in the negative z-direction, as seen in Fig. 5. The total number of grid points in the off-body grid is approximately 705 million grid points for $H/D = 1$ and 525 million points for $H/D = 0.5$, respectively, after 45 rotor revolutions. The domain size for the off-body is set to be 20 rotor radii away from the origin in every direction except in the negative z-direction due to the presence of the ground plane. Two heights are set for the rotors above the ground plane: half rotor diameter ($H/D = 0.5$) and one rotor diameter ($H/D = 1$), as shown in Fig. 5.

Acoustic Simulation Setup

An acoustic prediction tool, PSU-WOPWOP [44, 45], is used for the acoustic predictions in this work. Farassat's Formulation 1A [46, 47, 48] of the Ffowcs Williams and Hawkings (FW-H) equation [49] was numerically implemented in PSU-WOPWOP. The impermeable surface approach is used in the present work.

In the acoustic simulations performed, for the single observer cases, an observer is positioned at the 90° elevation angle on the ground plane. Additionally, the effect of acoustic reflections off the ground is considered along with the aerodynamic influence of the ground. The acoustic reflections are simulated in PSU-WOPWOP using an image source method, creating a mirrored image of the SbS rotor below the ground plane at a distance equidistant to the SbS rotor located above the ground plane. For the multiple observer cases, a total of 2,500 ground observers are positioned in a rectangular grid on the ground plane

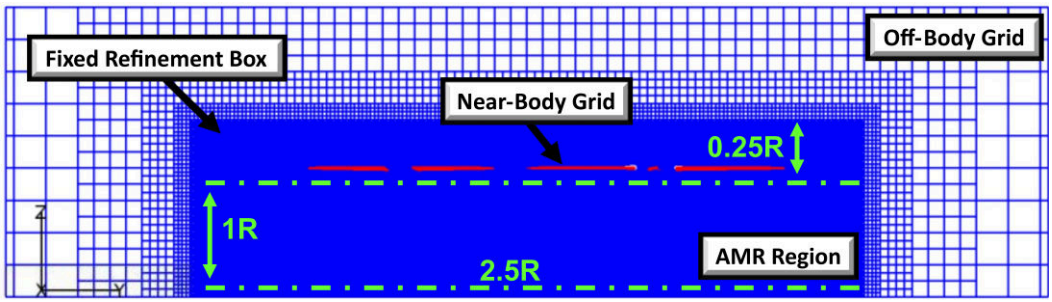

(a)

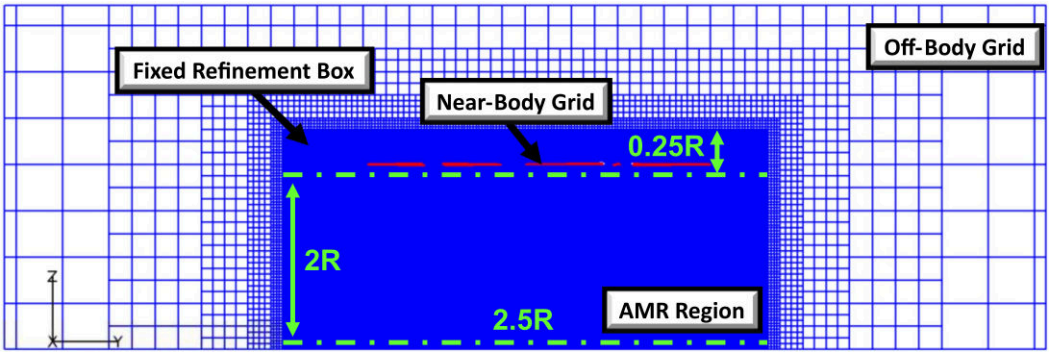

(b)

Fig. 5: Off-body grids for the IGE cases for 0% overlap case: (a) H/D = 0.5 and (b) H/D = 1.

for both overlap cases to study the noise directivity.

Results

In this section, the results for the performance, flow physics, aerodynamics, and aeroacoustics are presented for two different overlap configurations at two different heights.

Performance

The SbS rotor were simulated in hover for the 0% and 25% overlap configurations using OVERFLOW in Helios, taking into account the ground effect. The simulations were performed with a collective pitch angle of 8° for both overlap configurations. A total of 45 rotor revolutions (10,488 time steps) were run to ensure full development of the flow field as the wake from the combined rotor system progressed towards the ground.

For the overlapped cases, the definitions of the thrust and torque coefficients, is based on the projected area between two rotors in tandem from Johnson [50]. Let $A_{ov} = mA$ be the the overlap area, where A denotes a single rotor disk area, and m is defined as:

$$m = \frac{2}{\pi}\left[\cos^{-1}\frac{d}{2R} - \frac{d}{2R}\sqrt{1-\left(\frac{d}{2R}\right)^2}\right] \tag{1}$$

where d is the shaft separation distance as seen in Fig. 6. Then, the projected area is given as $A_{proj} = A(2-m)$. This equation has also been used in previous studies of the side-by-side rotor configuration [33, 51].

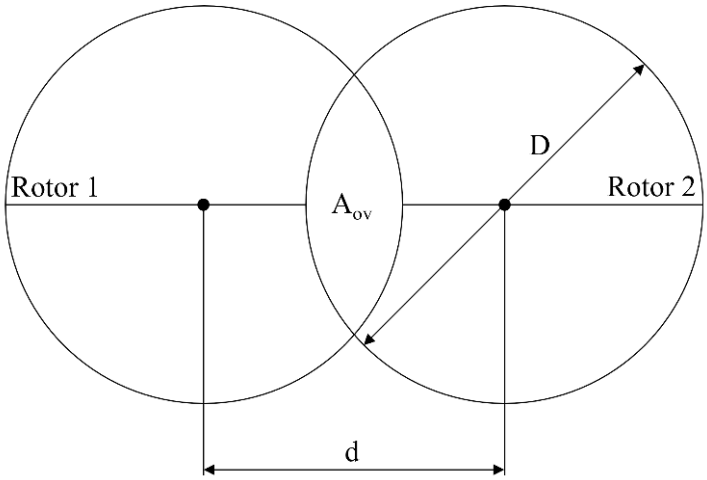

Fig. 6: Overlapping rotor geometry exhibiting the overlap area, A_{ov}

Figures 7 shows a comparison between IGE and OGE scenarios for both the thrust and torque coefficients generated by the combined rotors, in both the 0% and 25% overlap cases. Thrust and power increase as the rotor is positioned closer to the ground, with this effect being particularly pronounced for the 25% overlap cases. For the 0% overlap configuration, the same trend is observed at $H = 0.5D$. However, at $H = 1D$, the thrust remains nearly comparable to the OGE condition, indicating a negligible ground effect. Although there is a slight reduction in thrust at $H = 1D$ for the 0% overlap configuration compared to the OGE case, we attribute this to the flow unsteadiness effect. When comparing the 0% and 25% overlap scenarios, it can be observed that the 25% overlap scenario consistently results in higher values for both thrust and torque compared to the 0% overlap scenario.

Figure 8 displays the convergence of the Figure of Merit (FM) for the 0% and 25% overlap configurations, considering both rotor height cases of $H = 0.5D$ and 1D, at a collective pitch angle of 8°. The definition of FM can be found in Eq. (2), which was used in a recent study performed by Wright *et al.* [51] and Sagaga and Lee [29]. Similar to the thrust and torque coefficients, Eq. (2) uses the projected

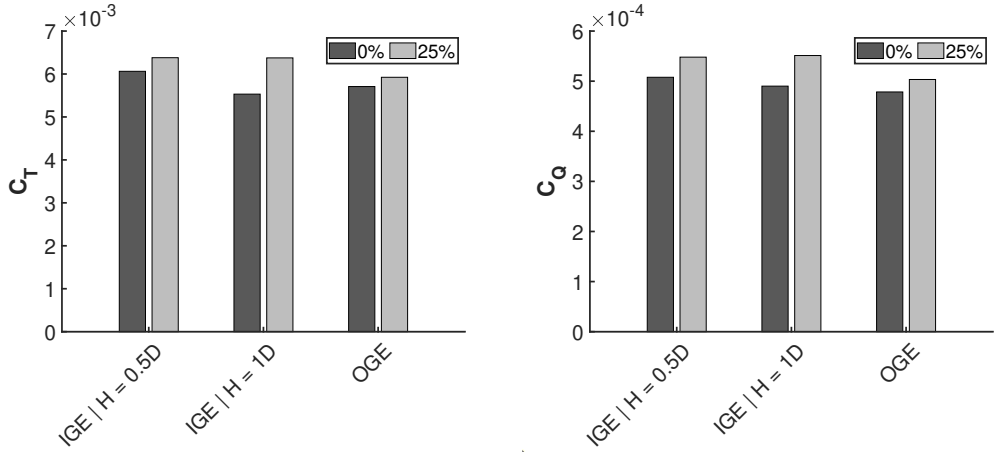

Fig. 7: Performance comparison between IGE and OGE for the 0% and 25% overlap cases: (a) thrust coefficient and (b) torque coefficient.

overlap area A_{proj}.

$$FM = \frac{T_{total}}{P_{total}} \sqrt{\frac{T_{total}}{2\rho A_{proj}}} \tag{2}$$

The convergence can be observed to be reached between 9 and 10 rotor revolutions in OGE and between 44 and 45 rotor revolutions in IGE. It is shown that the $H = 0.5D$ case results in a higher FM compared to $H = 1D$ for both configurations, but with increased and irregular fluctuations at the 0% overlap case. The 25% overlap case displays similar or more regular fluctuation magnitudes at both heights.

Table 4 presents the FM that is averaged over the last revolution for the 0% and 25% overlap configurations in both OGE and IGE scenarios, at a collective pitch of 8° for the combined rotors. The OGE cases for the 0% and 25% overlap configurations serve as the baseline for comparison with the IGE cases. The results show that the 0% overlap IGE case has a difference in FM ranging from about 15% to about 1% for rotor heights of $H = 0.5D$ and 1D, respectively. The 25% overlap IGE case has a difference in FM ranging from about 15% to about 2% for rotor heights of $H = 0.5D$ and 1D, respectively. The performance increase with the ground effect is similar for different overlap cases.. The detailed flow physics related to this performance difference will be examined in the next subsequent section.

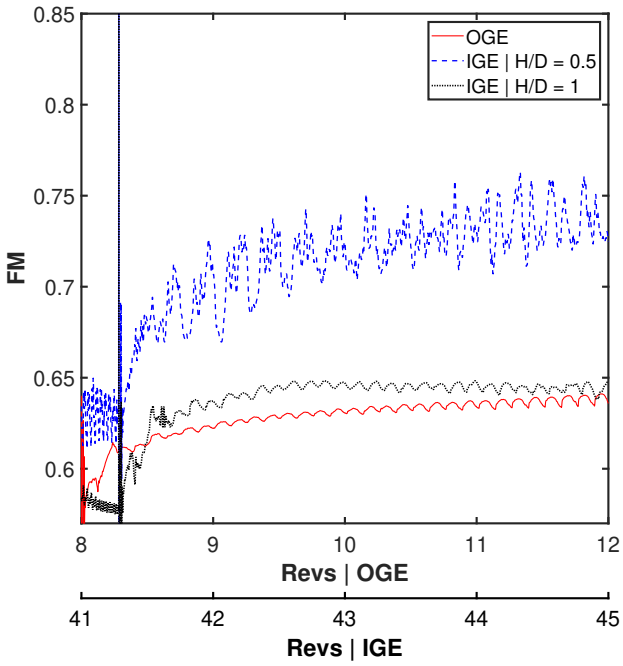

(a)

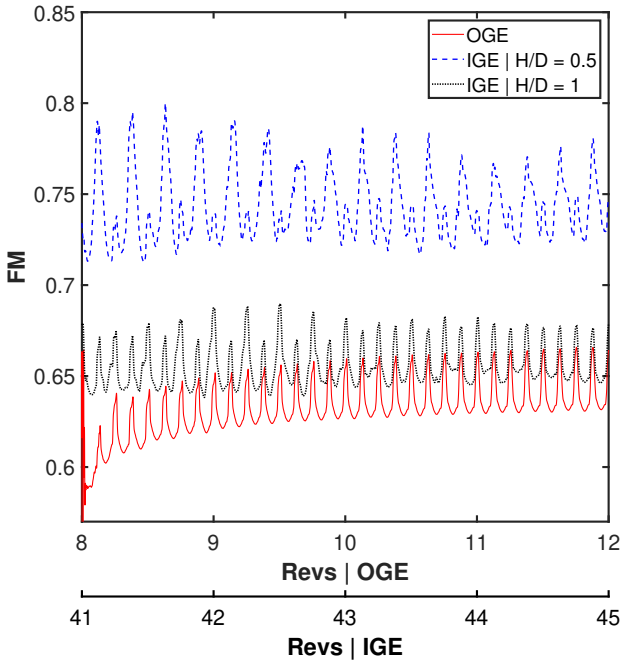

(b)

Fig. 8: Figure of merit convergence plots for the 0% and 25% overlap cases: (a) 0% overlap and (b) 25% overlap.

Flow Physics

Figures 9 and 10 depict the iso-surface of the q-criterion, colored with the vorticity magnitude for the 0% and 25% overlap cases with IGE and OGE at 8° collective. The figures also show the entrance

Table 4: FM that is averaged over the last revolution for 0% and 25% overlap cases for the combined rotors

Figure of Merit						
CP\OL	0% (OGE)	0% (H=0.5D)	0% (H=1D)	25% (OGE)	25% (H=0.5D)	25% (H=1D)
8°	0.637	0.735 (15.4%)	0.644 (1.1%)	0.640	0.742 (15.9%)	0.657 (2.5%)

and exit regions of the overlap for the right rotor. In the 25% overlap configuration, there is a clear interaction between the tip vortices from the left rotor and right rotor blades at the entrance and exit regions at the given time step, which is a major source of noise and will be discussed in detail later. After this interaction, the tip vortices break down and become less discernible. The wake development exhibits significant differences for each case, including the influence of not only the overlap region but also the ground plane on the overall formation of the wake. It is shown that the vortices near the hub of each rotor move upwards, as well as the overlap entrance and exit regions at a rotor height of $H = 0.5D$, with the effect being more noticeable in the 0% overlap case than the 25% overlap case. In the outwash region, the flow transitions from mostly vertical to a radial outwash as it strikes the ground plane, developing into a radial wall jet moving away from the wake of both rotors, as evidenced by the radial spread of wakes. Additionally, smaller worm-like structures are observed especially for OGE, which have been identified as secondary vortex structures and previously investigated in studies of isolated rotor cases [52, 53, 54]. The number of secondary vortex structures decreases as the rotors approach the ground. In other words, the wakes become more stabilized when the rotors operate near the ground.

Figures 11 and 12 provide a comparison of the induced inflow ratio at the rotor center plane for both IGE and OGE cases of the 0% and 25% overlap configurations. The inflow ratio is defined in Eq. (3) [55]:

$$\lambda_h = \lambda_i = \frac{v_i}{\Omega R} \tag{3}$$

where v_i is the induced velocity, Ω is the angular velocity, and R is the rotor radius. The positive value (red color) indicates the upwash and the negative value (blue color) indicates the downwash. The figures show a substantial increase in upwash flow, as indicated in Figs. 11(b), 11(c), 12(b), and 12(c) for IGE cases, especially in the hub region. If the physical structure at the hub location were included, this upwash in the hub region might be mitigated. However, it will be demonstrated that the inboard section near the hub

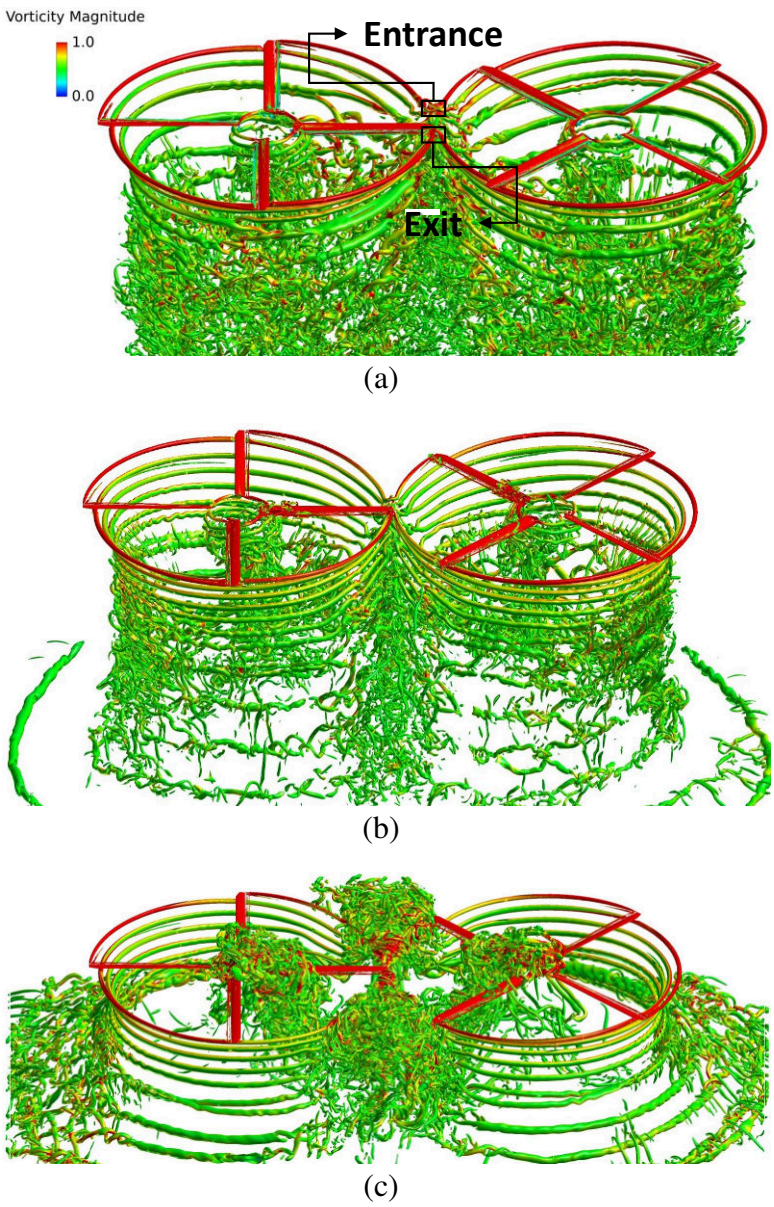

Fig. 9: Iso-surfaces of the q-criterion with the vorticity magnitude for the 0% overlap case: (a) OGE, (b) $H = 1D$, and (c) $H = 0.5D$.

does not significantly contribute to the aerodynamics and aeroacoustics. Therefore, accurate modeling of the hub region may not be necessary for the current study.

Both IGE cases of the 0% overlap configuration generate more upwash than IGE cases of the 25% overlap configuration. The downwash significantly increases in the overlap region in the 25% overlap configuration due to the overlapped tip vortices and wake effects from each rotor. The downwash is high and pushes the blade tip vortices downward, leading to reduced upwash in the overlap region for the IGE

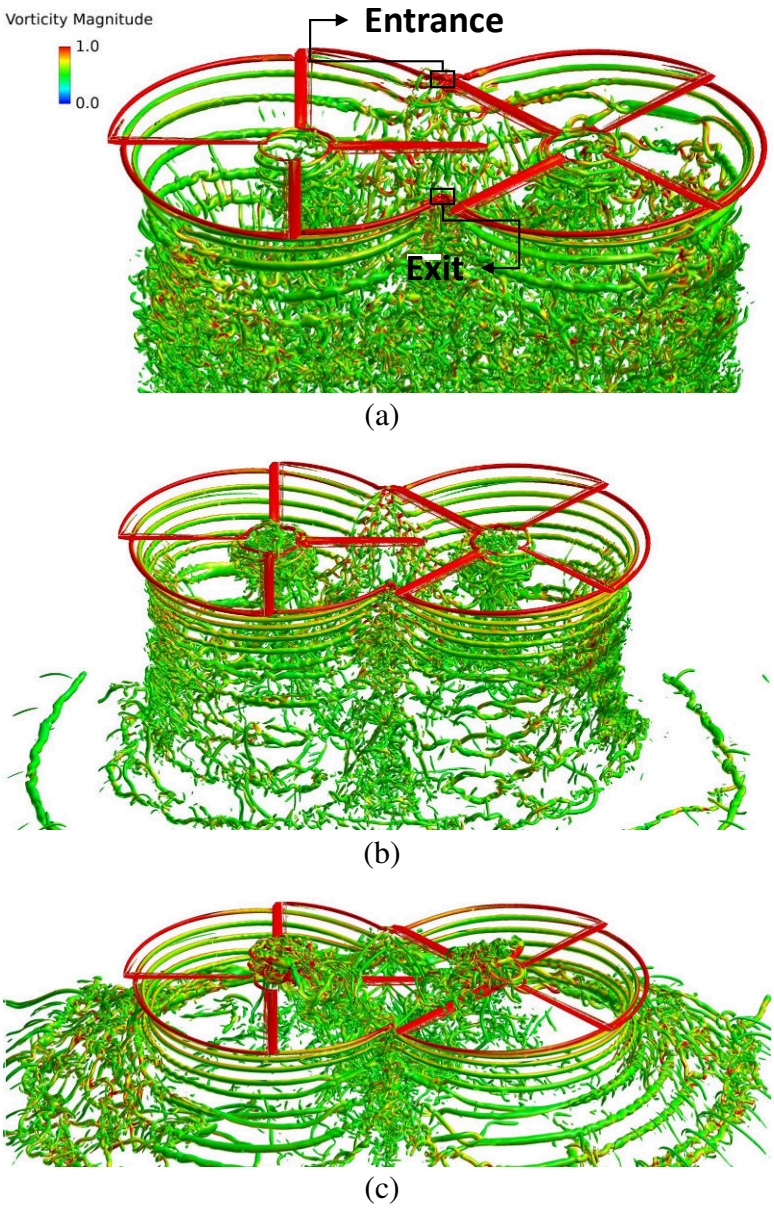

Fig. 10: Iso-surfaces of the q-criterion with the vorticity magnitude for the 25% overlap case: (a) OGE, (b) $H = 1D$, and (c) $H = 0.5D$.

cases of the 25% overlap configuration. This demonstrates the effect of overlap on the upwash influenced by the ground plane. As the rotor height increases for the IGE cases of both overlap configurations, the amount of upwash decreases in both the hub and overlap regions. For the 25% overlap configuration, changing the rotor height from $H = 0.5D$ to $H = 1D$ results in an even greater increase in downwash, comparable to OGE of the 25% overlap case. However, there is a similarity between the scenarios of 0% overlap at $H = 0.5D$ (Fig. 11(c)) and 25% overlap at the same height (Fig. 12(c)), with both showing

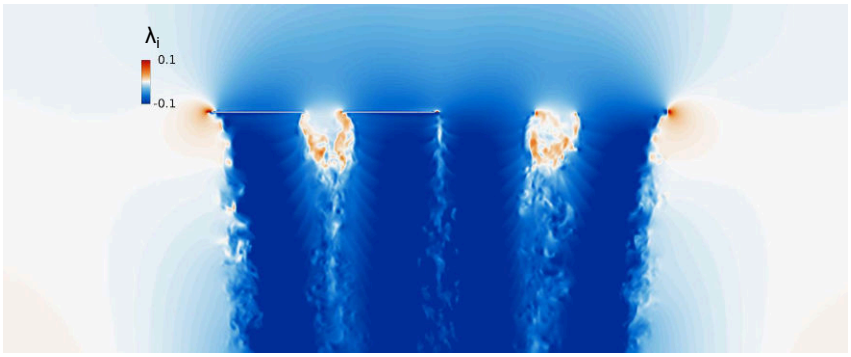

(a)

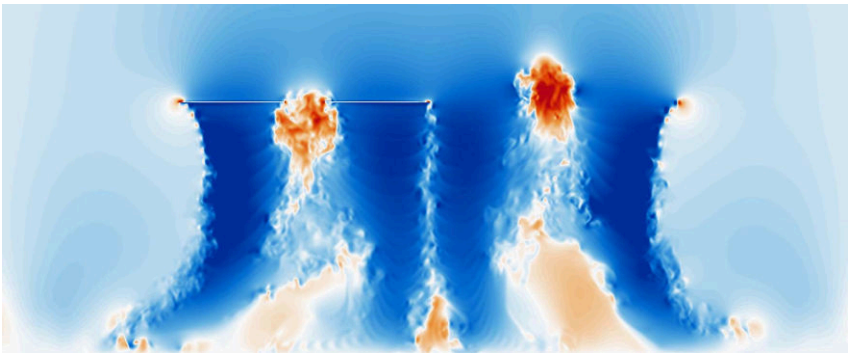

(b)

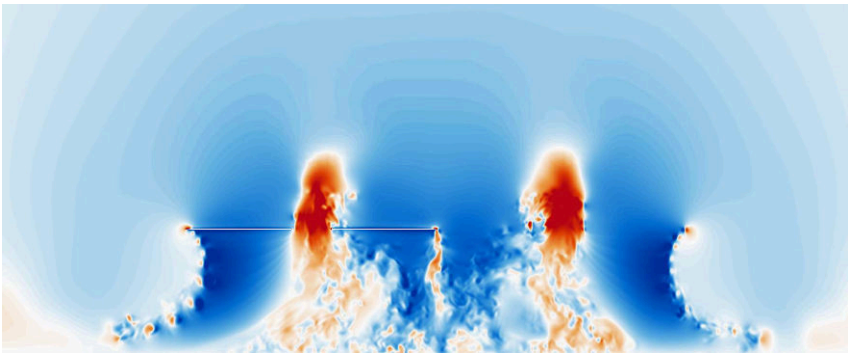

(c)

Fig. 11: Comparison of λ_i (inflow ratio) between the OGE and IGE cases for the 0% overlap configuration. The black bar represents the rotor disk plane: (a) OGE, (b) $H = 1D$, and (c) $H = 0.5D$.

higher upwash. This suggests that at $H = 0.5D$, the ground effect is more influential than the overlap effect.

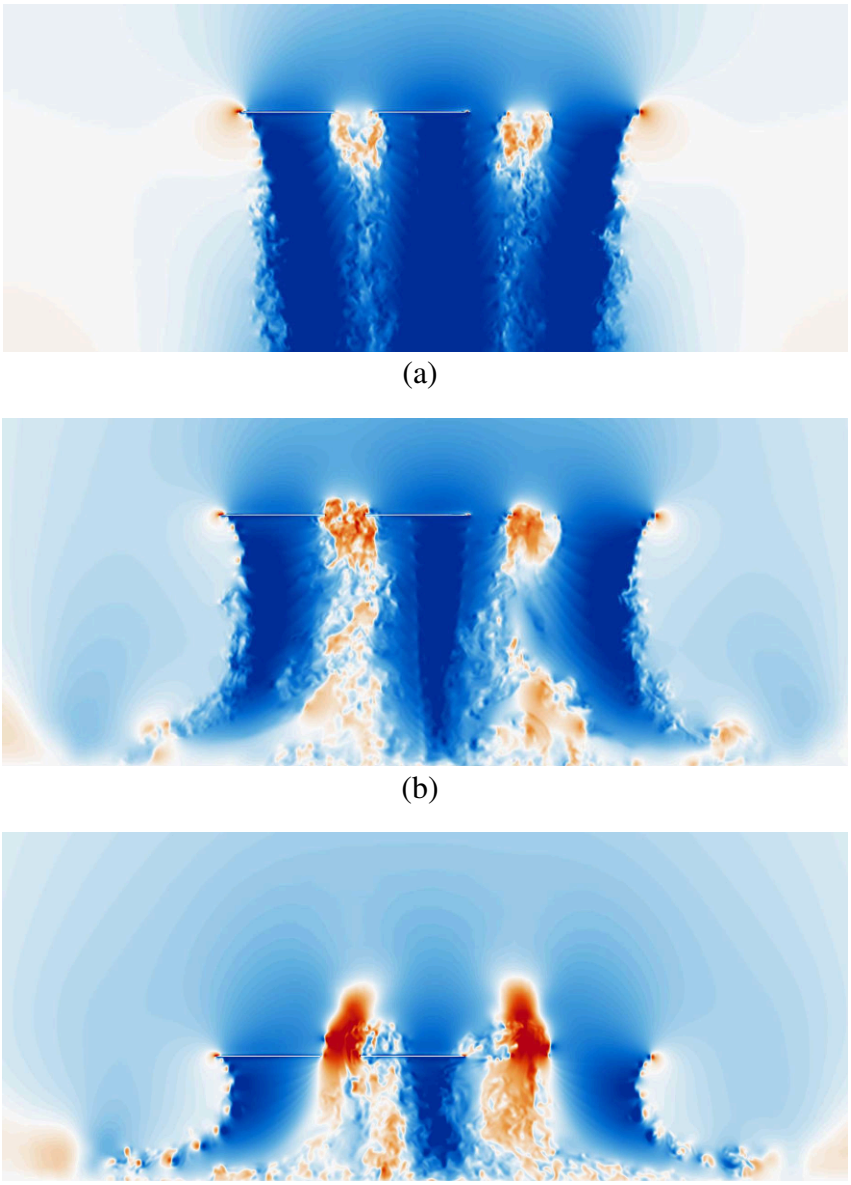

(a)

(b)

(c)

Fig. 12: Comparison of λ_i (inflow ratio) between the OGE and IGE cases for the 25% overlap configuration. The black bar represents the rotor disk plane: (a) OGE, (b) $H = 1D$, and (c) $H = 0.5D$.

Hazardousness Factor

The hazardousness factor is an important metric in terms of evaluating the safety and performance of rotorcraft operations near the ground, and it is determined based on the velocity parallel to the ground plane, encompassing both the time-average and standard deviation [22, 56] as follows:

$$f_h = ||\overline{\mathbf{u}}^{||}|| + \beta \mathbf{u}^{||}_{\mathbf{std}} \tag{4}$$

where $||\overline{\mathbf{u}}^{||}||$ indicates the time-averaged parallel velocity on the ground and $\mathbf{u}^{||}_{\mathbf{std}}$ represents the standard deviation. The parameter β set to 1.0. Previous studies [22, 56] have demonstrated that rotor height significantly influences the hazardousness factor due to the increase in induced velocity and the decrease in upwash.

Figures 13 and 14 shows the hazardousness factor for the two IGE and two overlap cases as a function of the radial distance on the ground. The 25% overlap case exhibits a higher hazardousness factor due to a stronger downwash effect at both heights. At a height of $H = 0.5D$, the trend of the hazardousness factor is opposite between the 0% and 25% overlap cases as x/D increases. This is attributed that, in the 25% overlap case, the strong downwash at the rotor vehicle center produces significant parallel velocity, which diminishes outward. In contrast, in the 0% overlap case, the downwash is weaker, and the rotor blades are more extended outward, resulting in more pronounced ground-parallel velocity flow at outward locations. For $H = 1.0D$, the trend of the hazardousness factor for the two overlap cases is similar, both increasing as x/D increases. The difference between the two cases is smaller compared to $H = 0.5D$, indicating that the effect of overlap on the hazardousness factor plays a minor role as the distance from the ground increases. Overall, the hazardousness factor is higher for $H = 0.5D$ than for $H = 1.0D$, and 25% overlap shows higher safety concerns near the ground than 0% overlap.

Aerodynamics

We investigate the variation in aerodynamics between the IGE and OGE cases of the 0% and 25% overlap configurations, with a focus on the overlap region. Figures 15 and 16 show the normal force only for the left rotor disk. For the out-of-ground and $H = 1D$ cases, a decrease in the normal force magnitude

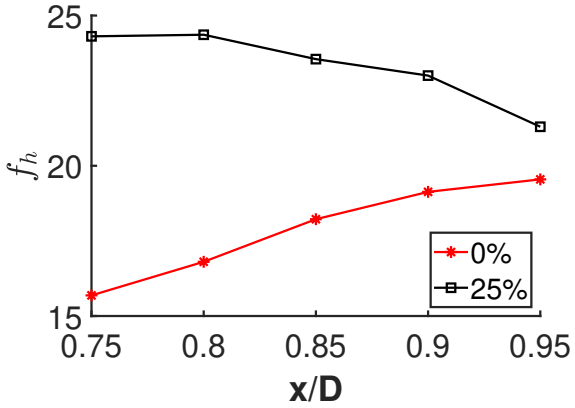

Fig. 13: Hazardousness for the IGE cases of the 0% and 25% overlap configuration at $H = 0.5D$.

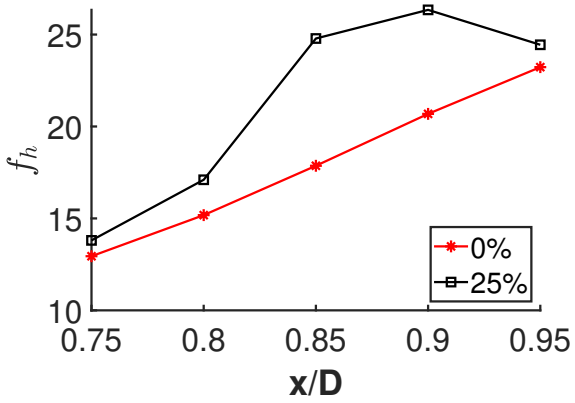

Fig. 14: Hazardousness for the IGE cases of the 0% and 25% overlap configuration at $H = 1D$.

occurs at ψ = 270°, where the influence of the right rotor is dominant in all 0% and 25% overlap cases. At the 25% case, the impact of overlap becomes more pronounced, as evidenced by the greater azimuthal range in which the thrust deficit arises. Figures 15(c) and 16(c) depict the increase in the normal force in the middle and outer regions of the rotor disk, but more noticeably near the overlap region at $H = 0.5D$ due to the strong upwash effect as discussed in the previous subsection, especially notable in the 0% case.

Figures 17 and 18 depict the non-dimensional normal force as a function of azimuthal angle at four radial locations ($r/R = 0.5, 0.75, 0.9$, and 1.0). The figures compare the normal force for the IGE and OGE cases of the 0% and 25% overlap configurations. The width, depth, and rate of change of the normal force increase significantly with increasing overlap, as seen in the 25% overlap configuration. At $r/R = 0.5$, $H = 0.5D$ significantly increases the normal force for both configurations. This increase is significant and leads to an improvement in thrust performance as discussed earlier. At the outboard

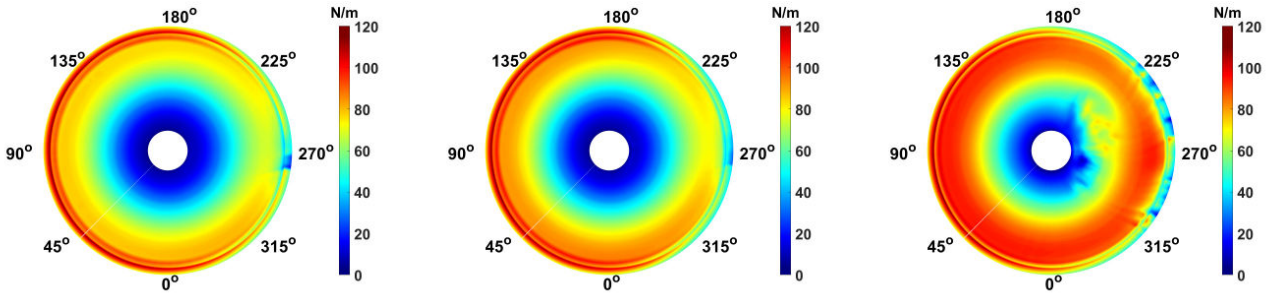

(a) (b) (c)

Fig. 15: Normal force for the 0% overlap configuration comparing the in- and out-of-ground effect cases: (a) OGE, (b) $H = 1D$, and (c) $H = 0.5D$.

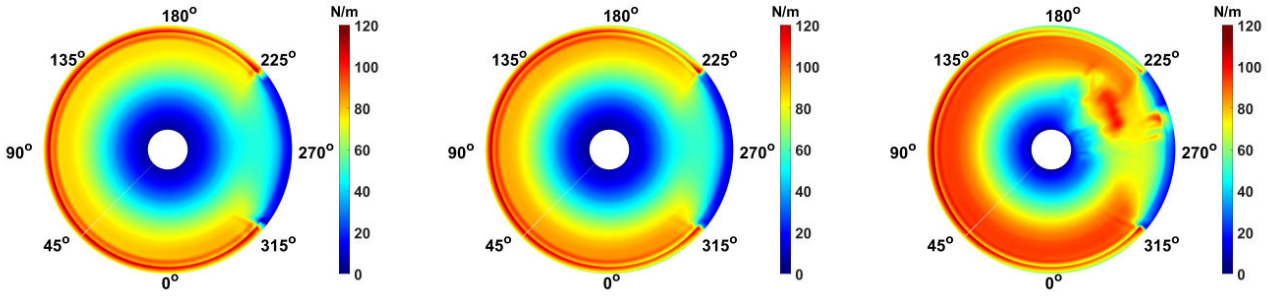

(a) (b) (c)

Fig. 16: Normal force for the 25% overlap configuration comparing the in- and out-of-ground effect cases: (a) OGE, (b) $H = 1D$, and (c) $H = 0.5D$.

locations, sharp peaks and fluctuations appear for the both configurations at $H = 0.5D$. However, as noted in the previous subsection, at $H = 1D$, both overlap cases show performance similar to the out-of-ground effect cases in the overlap region, although the OGE case shows smaller normal forces than $H = 1D$ outside the overlap region.

In Fig. 19, the blade sectional thrust coefficient is presented for the IGE cases of the 0% and 25% overlap configurations at azimuthal angles of 0°, 90°, 180°, and 270°. There is a deficit in the sectional thrust that is more prominent at the 270° azimuthal angle, which increases as the overlap region expands. At $H = 0.5D$, the decrease in the sectional thrust at the 270° azimuthal angle is not noticeable, especially at the 0% overlap configuration. At the 25% overlap configuration, the decrease in the sectional thrust is more noticeable in both in-ground cases. The decrease in sectional thrust correlates with the normal force distribution shown in Figs. 15 and 16. The reduced thrust at the 25% configuration is due to the increased induced velocities caused by the two rotor tip vortex effects observed in Figs. 11 and 12. Due

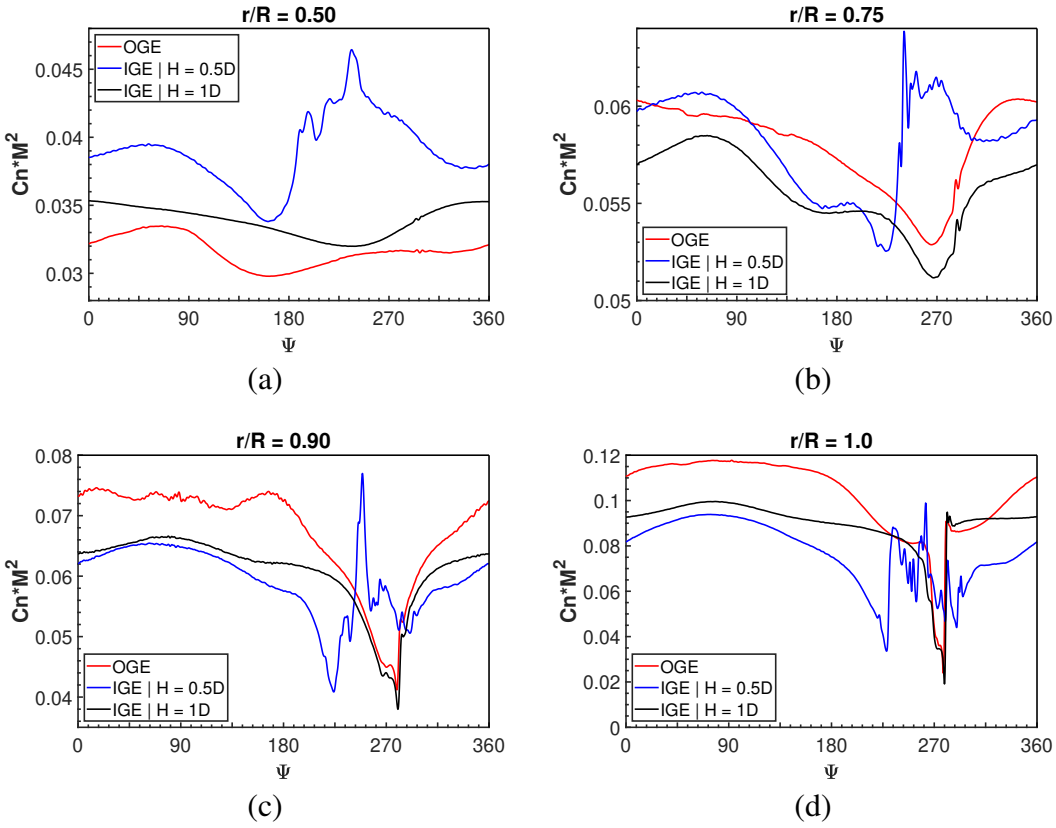

Fig. 17: The non-dimensional normal force coefficient for the 0% overlap at four different radial locations: (a) $r/R = 0.5$, (b) $r/R = 0.75$, (c) $r/R = 0.90$, and (d) $r/R = 1.0$.

to the periodic variation of rotor thrust with azimuthal angle, FM oscillates, as demonstrated in Fig. 8.

Aeroacoustics

Acoustic results, including the acoustic pressure time histories and sound pressure spectra, are obtained using PSU-WOPWOP. The sound pressure spectra are obtained using the standard Fast Fourier Transform method, applied to the data from the last rotor revolution, without the use of a window function or band-pass filtering. The surface pressure data necessary for the acoustic simulations are extracted as patches from the CFD grids of each rotor blade during the CFD simulation. The extracted patches are then converted into an amenable format for PSU-WOPWOP.

Figure 20 shows a quantitative comparison of $dF_z/d\Psi$ of the left rotor at the 75% span for all OGE and IGE cases of the 0% and 25% overlap configurations. This azimuthal or temporal derivative of the normal force is the main source of the loading noise of Farassat's Formulation 1A [47]. It is clear that the pressure

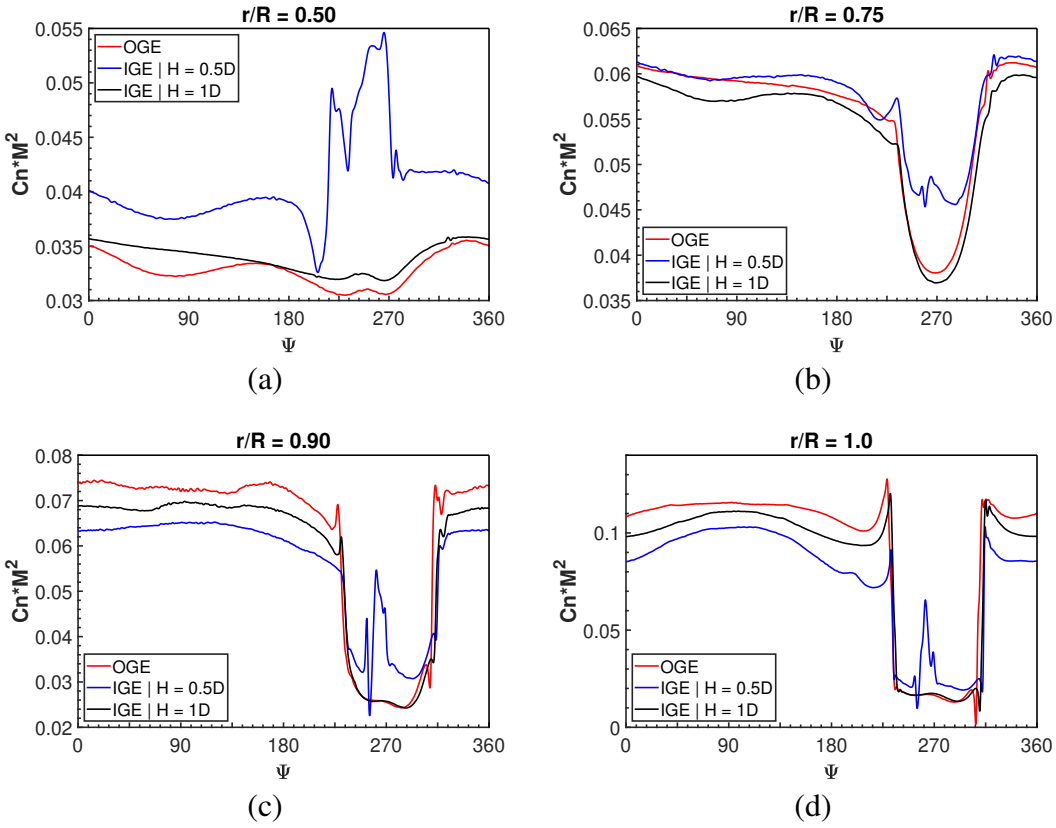

Fig. 18: The non-dimensional normal force coefficient for the 25% overlap at four different radial locations: (a) $r/R = 0.5$, (b) $r/R = 0.75$, (c) $r/R = 0.90$, and (d) $r/R = 1.0$.

fluctuation events are located within 225° and 315° azimuths where there are strong aerodynamic events due to interaction between the upwash flow and rotor blades as well as rotor-to-rotor interactions. Some of the rotor-to-rotor interactions include the interaction between the wake or vortices from one rotor with the other especially near the overlap entrance and exit regions as seen in Figs. 9 and 10. In Fig. 20(a), at about the 290° azimuth angle for the 0% overlap configuration at $H = 0.5D$, there are peaks with a significantly large amplitude compared to the peaks in the 25% overlap case. The flow upwash interacting with blades at the 0% overlap IGE and $H = 0.5D$ case contributes to the strongest pressure fluctuations, which is similar to a full SbS vehicle case including fuselage in OGE case [30]. For the 25% case, three results are very similar, although $H = 0.5D$ shows a higher amplitude near the entrance region.

Figure 21 shows the total acoustic pressure of a single observer positioned below the rotor disk plane for $H = 0.5D$ and $H = 1D$, for both the 0% and 25% overlap configurations. The IGE and OGE cases are included. The tonal peaks appear regularly during the entrance and exit of the overlap for all

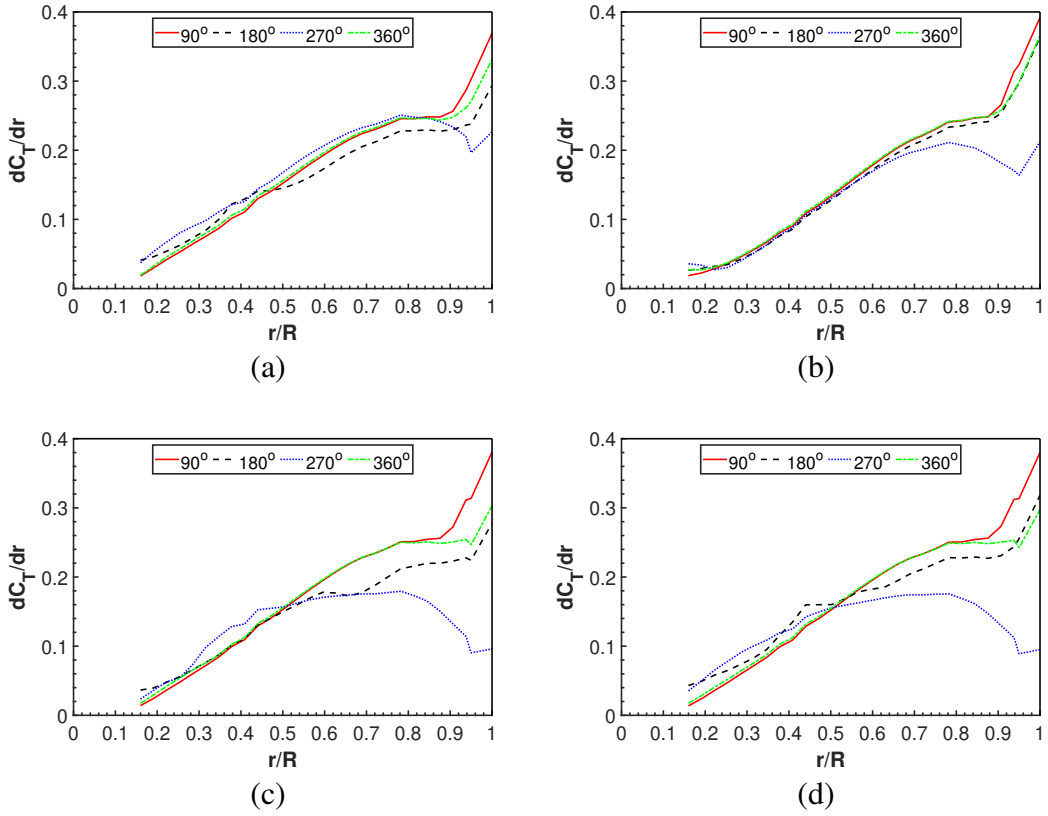

Fig. 19: Blade sectional thrust coefficient for the IGE cases: (a) 0% overlap at $H = 0.5D$, (b) 0% overlap at $H = 1D$, (c) 25% overlap at $H = 0.5D$, and (d) 25% overlap at $H = 1D$.

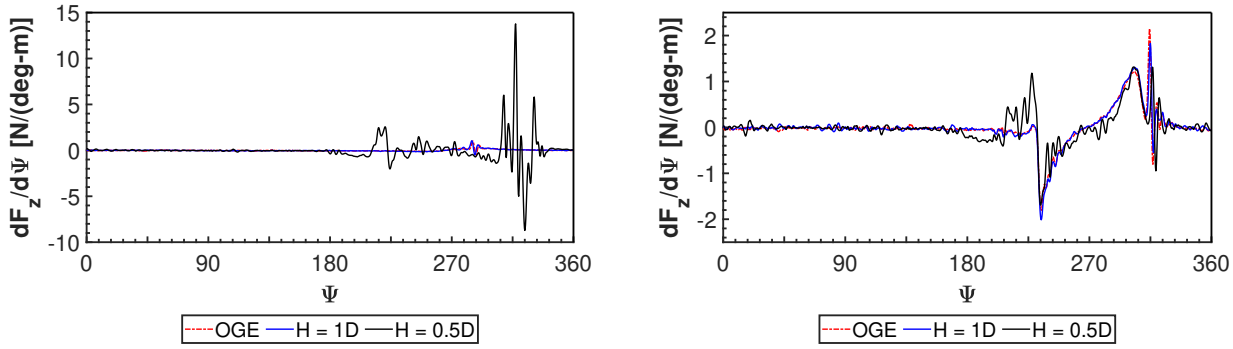

Fig. 20: Comparison of $dF_z/d\Psi$ of the left rotor at the 75% span for the IGE and OGE cases of the 0% and 25% overlap configurations: (a) 0% overlap and (b) 25% overlap.

the cases, except IGE cases at $H = 0.5D$ where there are irregular and multiple peaks. The additional frequency content present in the $H = 0.5D$ cases are mainly due to the upwash effect as discussed. For

the 0% configuration, IGE with $H = 1D$ and OGE with $H = 0.5D$ give similar acoustic amplitudes but with different phases. OGE with $H = 1D$ yields the lowest acoustic amplitude. In the case of the 25% configuration, IGE with $H = 1D$ and OGE with $H = 1D$ provide similar results, indicating reduced ground effect for larger overlap and $H = 1D$.

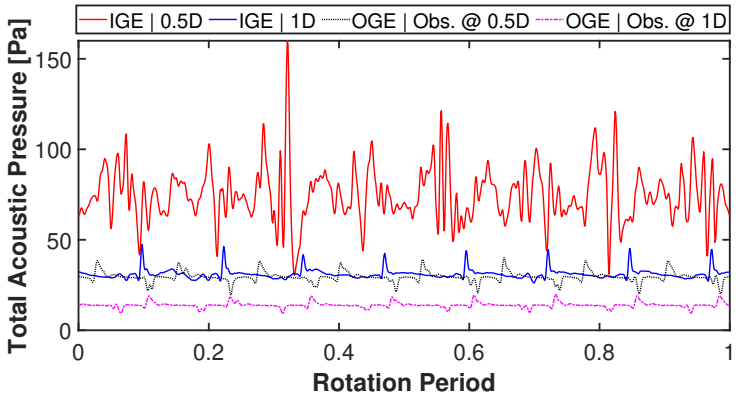

(a)

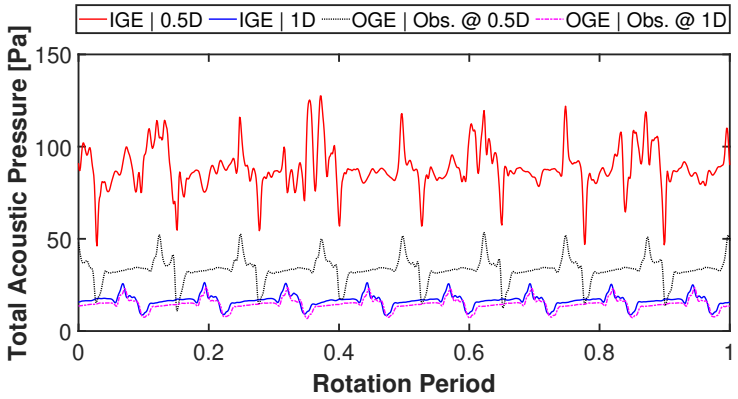

(b)

Fig. 21: Comparison of the total acoustic pressure for IGE and OGE cases of the 0% and 25% overlap configurations: (a) 0% overlap and (b) 25% overlap. Observers are located on the ground directly below the hub center of the vehicle.

The A-weighted sound pressure level (SPL) for the first 50 blade passing frequency (BPF) harmonics is depicted in Fig. 22. For the OGE cases, even harmonics represent the dominant tonal frequencies, suggesting the presence of rotor-to-rotor interaction noise. In contrast, for the IGE cases at $H = 0.5D$, the tonal noise increases at both even and odd harmonics. This implies that the dominant noise sources include not only the rotor-to-rotor interaction noise but also the rotor and upwash flow interaction noise at each rotor, as illustrated in Fig. 21. At $H = 1D$, even harmonics remain dominant; however, the

magnitude for the IGE cases surpasses that of the OGE cases after the 25th harmonics at the 0% overlap configuration, and both cases exhibit similar results at the 25% configuration.

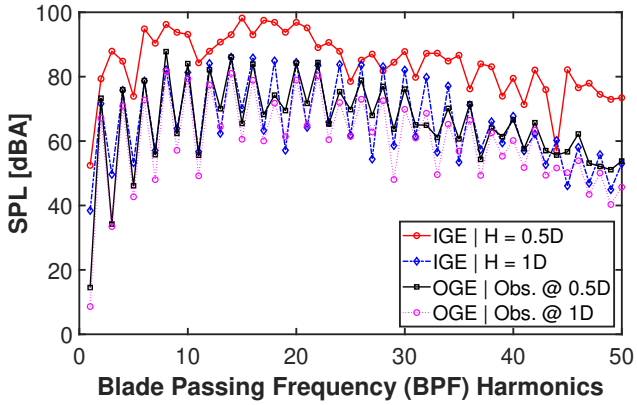

(a)

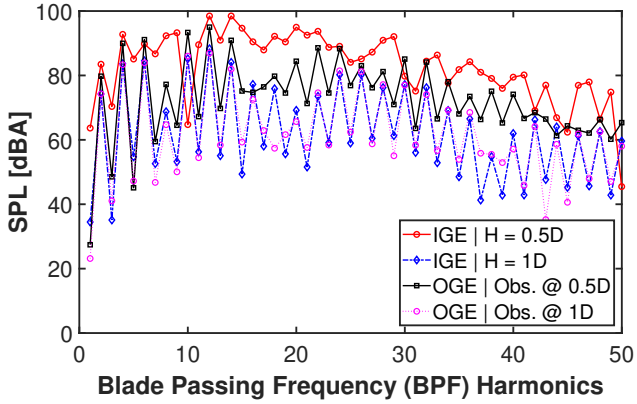

(b)

Fig. 22: Comparison of A-weighted SPL for the IGE and OGE cases of the 0% and 25% overlap configurations: (a) 0% overlap and (b) 25% overlap.

In order to diagnose the noise sources further, the contours of the first integrand of the loading noise portion of Farassat's Formulation 1A [47] is shown in Fig. 23 for the left rotor. This plot was first devised by Jia and Lee [4] to investigate the loading noise sources in SbS rotor in forward flight. The black lines in the contour plots represent the rotor blades at an observer time (black solid lines) when the acoustic peaks are observed. It is noted that, at the given microphone position, for the IGE cases at $H = 1D$ for both overlap configurations, the primary aerodynamic interactions are rotor-to-rotor BVI events occurring when the blades enter (blue color) or exit (red color) the overlap region. However, for the $H = 0.5D$ IGE cases in both overlap configurations, numerous interactions associated with upwash

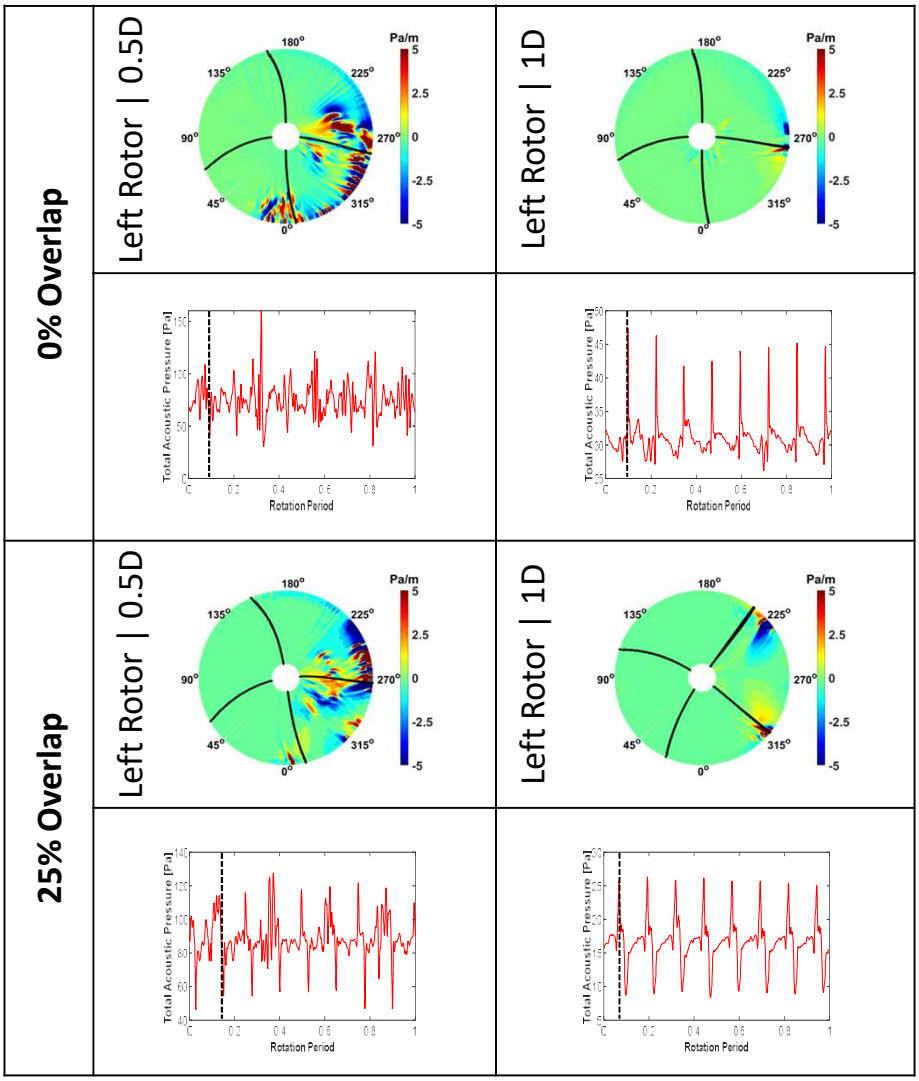

Fig. 23: Comparison of noise intergrand results of the left rotor for all IGE cases of the 0% and 25% overlap configurations.

flows other than rotor-to-rotor interactions are present, as discussed earlier. In particular, the $H = 0.5D$ cases exhibit significantly greater impulsiveness compared to the strength of the rotor-to-rotor BVI events in the $H = 1D$ cases. Figure 23 provides further evidence of the noise sources represented in Figs. 21 and 22

Figure 24 shows the A-weighted overall sound pressure level (OASPL) for all IGE cases of both the 0% and 25% overlap configurations, as well as the OGE cases. It can be observed that for both overlap configurations, the $H = 0.5D$ cases with IGE exhibit the highest OASPL compared to the other cases, due to the additional noise sources mentioned earlier. For the 0% overlap configuration, the $H = 1D$ case

with IGE demonstrates a higher noise level than the OGE case. Conversely, for the 25% configuration case, there is minimal difference between the IGE at $H = 1D$ and OGE at $H = 1D$ cases. In other words, the ground effect diminishes for the 25% overlap configuration after $H = 1D$ due to a strong downwash effect. Additionally, when the ground is absent, the 25% configuration results in higher noise levels than the 0% configuration for both heights. However, when the ground is present, this trend reverses.

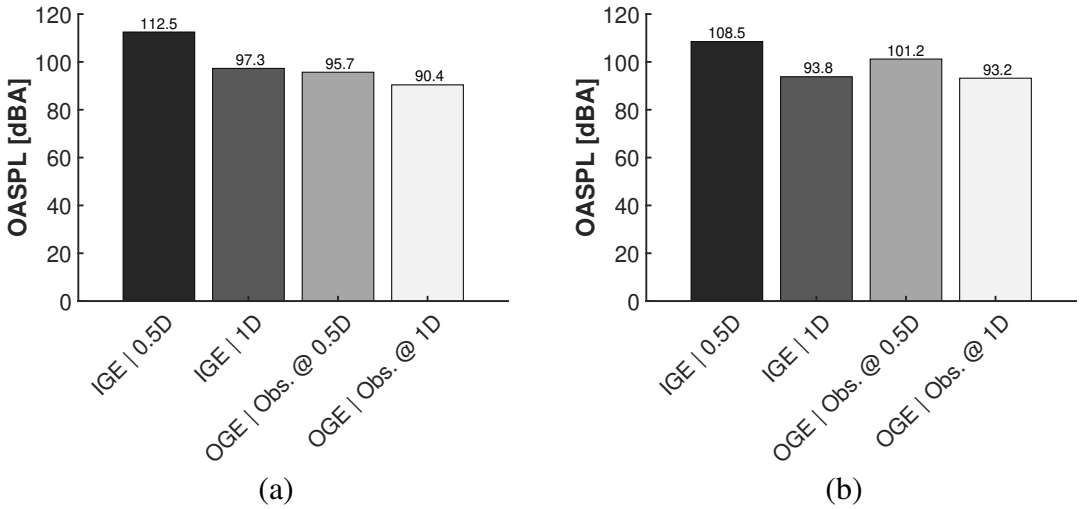

Fig. 24: Comparison of A-weighted OASPL for the IGE and OGE cases of the 0% and 25% overlap configurations: (a) 0% overlap and (b) 25% overlap.

Figure 25 illustrates the directivity between A-weighted and unweighted noise levels. The peaks and valleys in the unweighted noise levels arise due to constructive and destructive interference, primarily at the second harmonic waves. However, these low-frequency interferences are not evident in the A-weighted directivity. The A-weighted OASPL shows higher noise levels in the exit region of the right rotor (bottom) compared to the entrance region (top) (see Figs. 9 and 10), indicating the different noise directivity for different harmonics. For the 25% overlap configuration at $H = 1D$, the A-weighted OASPL reveals interference patterns in the exit region, which also occur in the unweighted region with a lower amplitude. This indicates that the interference mainly takes place at high frequencies in this case.

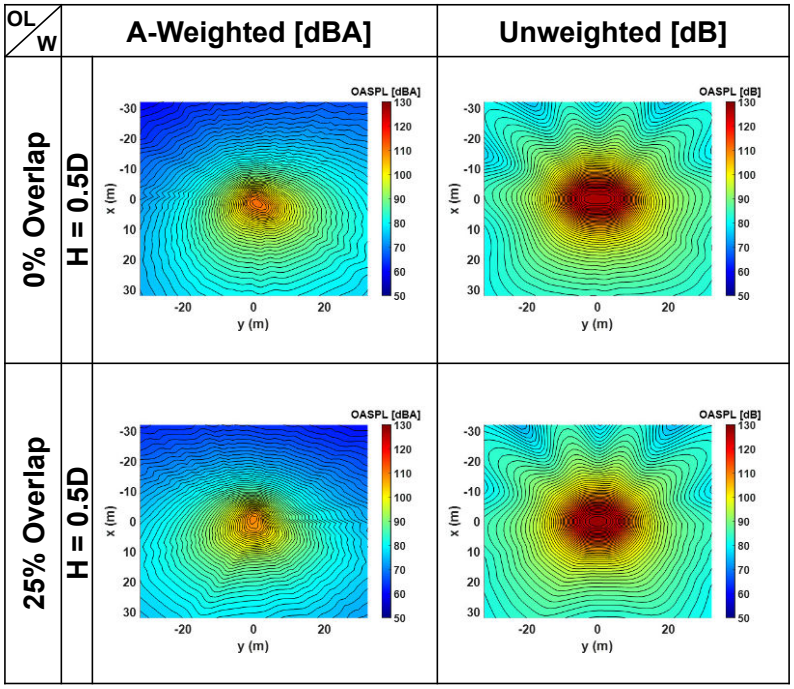

(a)

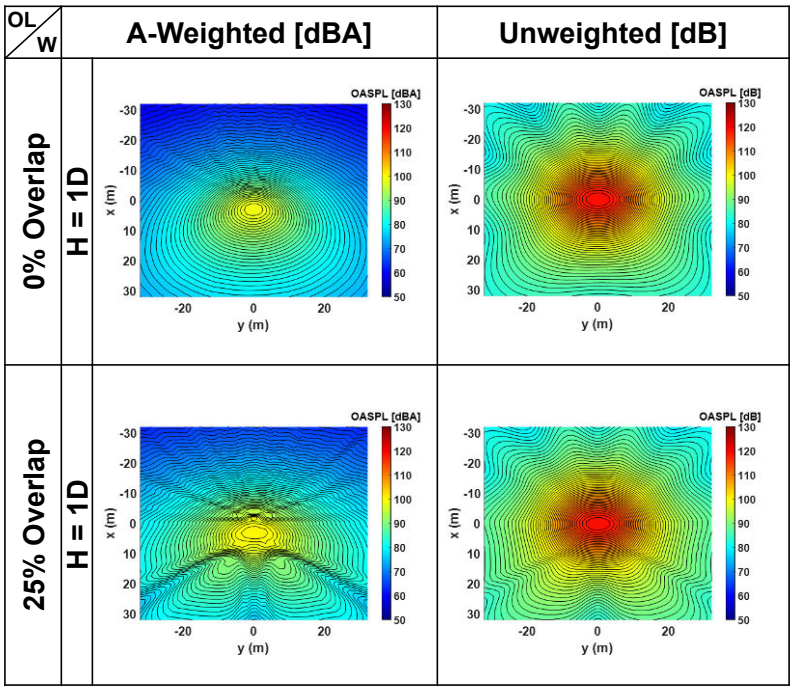

(b)

Fig. 25: Noise directivity (A-weighted and unweighted) for all IGE cases of the 0% and 25% overlap configuration: (a) $H = 0.5D$ and (b) $H = 1D$.

Conclusions

The impact of the ground surface on the six-passenger SbS rotors of NASA's UAM reference vehicle has been examined and analyzed in hover. High-fidelity CFD simulations were conducted using CREATE^{TM}-AV Helios to investigate the performance, aerodynamics, and acoustics with 0% and 25% overlap in both IGE and OGE cases. Acoustic simulations using an impermeable approach were performed with the acoustic prediction tool PSU-WOPWOP. Thrust, torque, and FM were first analyzed for different IGE cases at two rotor heights of $H = 0.5D$ and $H = 1D$. Tip vortex and induced velocity were also studied. The hazardousness factor were investigated for the safety concern. The effect of the ground surface on blade sectional aerodynamic loads was investigated, and connections between various acoustic sources and the resulting noise were examined for each IGE case. Directivity comparisons were made between both overlap configurations at $H = 0.5D$ and $H = 1D$. Based on the results presented and analyzed in this study, the following conclusions can be drawn:

1) The presence of the ground surface has a clear impact on the hover performance, as evidenced by an increase in FM in all IGE cases for both the 0% and 25% overlap configurations. Specifically, for the 0% overlap configuration at $H = 0.5D$ and $H = 1D$, there is a significant increase of 15% and 1%, respectively, compared to the OGE case. Similarly, for the 25% overlap case at $H = 0.5D$ and $H = 1D$, there is a 15% and 2% increase, respectively, compared to the 25% overlap OGE case. The performance increase with the ground effect is similar for different overlap cases.

2) It was observed that the induced velocity decreases considerably in the overlap region for the $H = 0.5D$ cases and shows a slight increase in the $H = 1D$ cases for the 0% overlap configuration. In contrast, for the 25% overlap cases, the increase in the induced velocity was observed, thereby overshadowing the upwash generated.

3) The hazardousness factor was significantly influenced by both rotor height and rotor overlap, with a noticeable increase observed in 25% overlap case at $H = 0.5D$. As the distance from the ground increases, 25% and 0% overlap cases exhibited similar trends.

4) In the vicinity of the overlap region, an increase in normal force was observed for the $H =$

$0.5D$ case, in contrast to the decrease seen in the OGE effect cases. The increase in normal force, particularly for the 0% overlap case, can be attributed to the absence of overlap and the reduction in induced velocity due to the significant amount of upwash generated.

5) At $H = 1D$, the most dominant source of noise in hover condition was the blade-tip interaction with the tip vortical structures as the blade enters and exits the overlap region for both overlap configurations. At $H = 0.5D$, due to the closer proximity to the ground and the upwash effect especially at the 0% overlap configuration, there was an increase in the number of aerodynamic interactions, such as rotor-to-rotor and rotor and upwash, resulting in noise increase at all harmonics. For the 25% overlap configuration, the OASPL levels became similar between the IGE case at $H = 1D$ and the OGE case, while the 0% configuration showed higher noise levels IGE at $H = 1D$ compared to the OGE case. Overall, the 25% configuration provided about 3-4 dB noise reduction compared to the 0% configuration near the ground. This indicates the noise reduction benefit of SbS rotor configurations with overlap near the ground.

6) The directivity patterns were found to be considerably different between the A-weighted and unweighted OASPL. The peaks and valleys in the A-weighted OASPL were significantly reduced or not as visible, except for the A-weighted OASPL of the 25% overlap case at $H = 1D$ in the exit region.

We note that our work utilized a fixed collective pitch angle for the overlap configurations considered. It is also important to examine different collective pitch angles at the same thrust value, and this will be explored in future research.

References

[1]Thipphavong, D. P., Apaza, R., Barmore, B., Battiste, V., Burian, B., Dao, Q., Feary, M., Go, S., Goodrich, K. H., Homola, J., Idris, H. R., Kopardekar, P. H., Lachter, J. B., Neogi, N. A., Ng, H. K., Oseguera-Lohr, R. M., Patterson, M. D., and Verma, S., "Urban Air Mobility Airspace Integration Concepts and Considerations," Paper AIAA 2018-3676, Proceedings of the Aviation Technology, Integration, and Operations Conference, Atlanta, GA, June 25–29, 2018.

[2]Rimjha, M., Trani, A., and Hotle, S., "Urban Air Mobility: Preliminary Noise Analysis of Commuter

Operations," Paper AIAA 2021-3204, Proceedings of the AIAA Aviation 2021 Forum, Virtual Event, August 2–6, 2021.

[3]Jia, Z. and Lee, S., "Computational Study on Noise of Urban Air Mobility Quadrotor Aircraft," *Journal of the American Helicopter Society*, **67**, 012009 (2022), DOI: 10.4050/JAHS.67.012009.

[4]Jia, Z. and Lee, S., "High-Fidelity Computational Analysis on the Noise of a Side-by-Side Hybrid VTOL Aircraft," *Journal of the American Helicopter Society*, **67**, 022005 (2022), DOI: 10.4050/JAHS.67.022005.

[5]Li, S. and Lee, S., "Prediction of Urban Air Mobility Multirotor VTOL Broadband Noise Using UCD-QuietFly," *Journal of the American Helicopter Society*, **66**, 032004 (2021), DOI: 10.4050/JAHS.66.032004.

[6]Clero, F., Mortain, F., , Le Nabat, J., Weber, D., Cabannes, T., and Matthieu, S., "Acoustic Measurement of Manned Electrical Vertical Take-Off and Landing (e-VTOL) Aircraft," Paper AIAA 2024-3229, Proceedings of the AIAA/CEAS Aeroacoustics Conference, Rome, Italy, June 4–7, 2024.

[7]Pascioni, K., Watts, M., Houston, M., Lind, A., Stephenson, J., and Bain, J., "Acoustic Flight Test of the Joby Aviation Advanced Air Mobility Prototype Vehicle," Paper AIAA 2024-3036, Proceedings of the AIAA/CEAS Aeroacoustics Conference, Southampton, UK, June 14–17, 2022.

[8]Henderson, B. S., Cluts, J., Svetgoff, A. A., Jantzen, J., and Bennett, J., "Acoustic Measurements for the Moog S-250 Vehicle in Hover," Paper AIAA 2024-3275, Proceedings of the AIAA/CEAS Aeroacoustics Conference, Rome, Italy, June 4–7, 2024.

[9]Li, S. and Lee, S., "Acoustic Analysis and Sound Quality Assessment of a Quiet Helicopter for Air Taxi Operations," *Journal of the American Helicopter Society*, **67**, 032001 (2022), DOI: 10.4050/JAHS.67.032001.

[10]Pettingill, N. and Zawodny, N., "Identification and Prediction of Broadband Noise for a Small Quadcopter," Proceedings of the 75th Annual Forum of the Vertical Flight Society, Philadephia, PA, May 2019.

[11]Schiller, N., Pascioni, K., and Zawodny, N., "Tonal Noise Control Using Rotor Phase Synchronization," Proceedings of the 75th Annual Forum of the Vertical Flight Society, Philadephia, PA, May 2019.

[12]Sarojini, D., Ruh, M., Joshy, A. J., Yan, J., Ivanov, A., Scotzniovsky, L., Fletcher, A., Orndorff, N., Sperry, M., Gandarillas, V., Asher, I., Chambers, J., Gill, H., Lee, S., Cheng, Z., Rodrigues, G., Zhao,

S., Mi, C., Nascenzi, T., Cuatt, T., Winter, T., Guibert, A., Cronk, A., Kim, H., Meng, S., and Hwang, J., "Large-Scale Multidisciplinary Design Optimization of an eVTOL Aircraft using Comprehensive Analysis," Paper AIAA 2023-0146, Proceedings of the AIAA SciTech Forum, National Harbor, MD, January 23–27, 2023.

[13]Bain, J., Goetchius, G., and Josephson, D., "Flyover Noise Comparison Between Joby Aircraft and Similar Aircraft," Proceedings of the 78th Annual Forum of the Vertical Flight Society, Ft. Worth, TX, May 2022.

[14]Gill, H., Lee, S., Ruh, M., and Hwang, J., "Applicability of Low-Fidelity Tonal and Broadband Noise Models on Small-Scaled Rotors," Paper AIAA 2023-1547, Proceedings of the AIAA SciTech Forum, National Harbor, MD, January 23–27, 2023.

[15]Gonclaves, M. M., Golubev, V. V., Lyrintzis, A. S., and Mankbadi, R. R., "High-Fidelity Simulations of Vertiport Ground Effects on eVTOL Rotor Noise," Paper AIAA 2024-3333, Proceedings of the AIAA/CEAS Aeroacoustics Conference, Rome, Italy, June 4–7, 2024.

[16]Healy, R., McCauley, J., Gandhi, F., and Sahni, O., "A Computational Examination of Side-by-Side Rotors in Ground Effect," *Journal of the American Helicopter Society*, **68**, 012011 (2023), DOI: 10.4050/JAHS.68.032007.

[17]Smith, B., Healy, R., Gandhi, F., and Lyrintzis, A., "eVTOL Rotor Noise in Ground Effect," Proceedings of the 77th Annual Forum of the Vertical Flight Society, Virtual Event, May 2021.

[18]Araghizadeh, M. S., Sengupta, B., Lee, H., and Myong, R. S., "Aeroacoustic Investigation of Side-by-Side Urban Air Mobility Aircraft in Full Configuration with Ground Effect," *Physics of Fluids*, **36**, 087160 (2024), DOI: 10.1063/5.0221902.

[19]Wei, P., Chan, S. N., Lee, S., and Kong, Z., "Mitigating Ground Effect on Mini Quadcopters with Model Reference Adaptive Control," *International Journal of Intelligent Robotics and Applications*, **3**, pp. 283–297 (2019).

[20]Glauert, M. B., "The Wall Jet," *Journal of Fluid Mechanics*, Vol. 1, (6), March 1956, pp. 625–643, DOI: 10.1017/S002211205600041X.

[21]Ferguson, S. W., "Rotorwash Analysis Handbook – Development and Analysis," FAA TR FAAJRD-93/31, Washington, D.C., 1994.

[22]Preston, J., S, T., Keen, E., Silva, M., Calvert, M., Cardamone, M., Moulton, M., and Ferguson, S. W., "Rotorwash Operational Footprint Modeling," US Army TR RDMR-AF-14-02, 2014.

[23]Federico, R., George, B., and René, S., "Safety Analysis of Rotors in Ground Effect," *Aerospace Science and Technology*, **129**, 107655 (2022), DOI: 10.1016/j.ast.2022.107655.

[24]Jung, Y. S., Lee, B., and Baeder, J. D., "Prediction of HVAB Hovering Rotor Performance and Ground Effect using Mercury Framework," Paper AIAA 2024-0895, Proceedings of the AIAA SciTech Forum, Orlando, FL, January 8–12, 2024.

[25]George, M., Kisielowski, E., and Douglas, D. S., "Investigation of the Downwash Environment Generated by V/STOL Aircraft Operating in Ground Effect," US Army TR AD674644, Fort Eustes, VA, 1968.

[26]Stephenson, J. H., "Comparative Downwash and Simulated Forest Rescue Tests of the HH-3E, HH-53B and the XC-142A Aircraft," US Air Force TR AD827382, Wright-Patterson Air Force Base, OH, 1967.

[27]Johnson, W., Silva, C., and Eduardo, S., "Concept Vehicles for VTOL Air Taxi Operations," Proceedings of the Vertical Flight Society Technical Conference on Aeromechanics Design for Transformative Vertical Flight, San Francisco, CA, January 2018.

[28]Diaz, P., Johnson, W., Ahmad, J., and Yoon, S., "Computational Study of the Side-By-Side Urban Air Taxi Concept," Proceedings of the 75th Annual Forum of the Vertical Flight Society, Philadelphia, PA, May 2019.

[29]Sagaga, J. and Lee, S., "Performance, Aerodynamics, and Aeroacoustics of Side-by-Side Rotors Using High-Fidelity Computational Fluid Dynamics," *AIAA Journal*, **61**, pp. 5429–5445 (2023), DOI: 10.2514/1.J062955.

[30]Sagaga, J. and Lee, S., "High-Fidelity Computational Study of Aerodynamic Noise of Side-by-Side Rotor in Full Configuration," *Journal of Sound and Vibration*, **592**, 118607 (2024), DOI: 10.1016/j.jsv.2024.118607.

[31]Silva, C., Johnson, W., and Solis, E., "Multidisciplinary Conceptual Design for Reduced-Emission Rotorcraft," Proceedings of the Vertical Flight Society Technical Conference on Aeromechanics Design for Transformative Vertical Flight, San Francisco, CA, January 2018.

[32]Radotich, M., "Conceptual Design of Tiltrotor Aircraft for Urban Air Mobility," Proceedings of the Vertical Flight Society Technical Conference on Aeromechanics Design for Transformative Vertical Flight, San Jose, CA, January 2022.

[33]Diaz, P., Johnson, W., Ahmad, J., and Yoon, S., "The Side-by-Side Urban Air Taxi Concept," Paper AIAA 2019-2828, Procceding of the AIAA Aviation Forum, Dallas, TX, June 17–21, 2019.

[34]Silva, C. and Johnson, W., "Practical Conceptual Design of Quieter Urban VTOL Aircraft," Proceedings of the 77th Annual Forum of the Vertical Flight Society, Virtual Event, May 2021.

[35]Li, S. and Lee, S., "Prediction of Rotorcraft Broadband Trailing-Edge Noise and Parameter Sensitivity Study," *Journal of the American Helicopter Society*, **65**, 042006 (2020), DOI: 10.4050/JAHS.65.042006.

[36]Lee, S., Ayton, L., Bertagnolio, F., Moreau, S., Chong, T. P., and Joseph, P., "Turbulent Boundary Layer Trailing-Edge Noise: Theory, Computation, Experiment, and Application," *Progress in Aerospace Sciences*, **126**, 100737 (2021), DOI: 10.1016/j.paerosci.2021.100737.

[37]Sitaraman, J., Jayaraman, B., Datta, A., Potsdam, M., Wissink, A. M., Jain, R., Adamec, S., and Abras, J., *Helios User Guide*, HPCMP CREATE, Lorton, VA, 2016.

[38]Nichols, R. and Buning, P., *User's Manual for OVERFLOW*, NASA Langley Research Center, Hampton, VA, 2018.

[39]Jia, Z. and Lee, S., "Impulsive Loading Noise of a Lift-Offset Coaxial Rotor in High-Speed Forward Flight," *AIAA Journal*, **58**, pp. 687–701 (2019), DOI: 10.2514/1.J058295.

[40]Jia, Z., Lee, S., Sharma, K., and Brentner, K. S., "Aeroacoustic Analysis of a Lift-Offset Coaxial Rotor Using High-Fidelity CFD/CSD Loose Coupling Simulation," *Journal of the American Helicopter Society*, **65**, 012011 (2020), DOI: 10.4050/JAHS.65.012011.

[41]Jia, Z. and Lee, S., "Aerodynamically Induced Noise of a Lift-Offset Coaxial Rotor with Pitch Attitude in High-Speed Forward Flight," *Journal of Sound and Vibration*, **491**, 115737 (2021), DOI: 10.1016/j.jsv.2020.115737.

[42]Chaderjian, N. M., "A Quantitative Approach for the Accurate CFD Simulation of Hover in Turbulent Flow," *Journal of the American Helicopter Society*, **68**, 042009 (2023), DOI: 10.4050/JAHS.68.042009.

[43]Chan, W. M., Pandya, S. A., Rogers, S. E., Jensen, J. C., Lee, H. C., Kao, D. L., Buning, P. G., Meakin, R. L., Boger, D. A., and Nash, S. M., *Chimera Grid Tools User's Manual*, NASA Ames Research Center, Mountain View, CA, 2018.

[44]Brès, G. A., Brentner, K. S., Perez, G., and Jones, H. E., "Maneuvering Rotorcraft Noise Prediction," *Journal of Sound and Vibration*, Vol. 275, (3), August 2004, pp. 719–738, DOI: 10.1016/j.jsv.2003.07.005.

[45]Lee, S., Bretner, K., Farassat, F., and Morris, P. J., "Analytic Formulation and Numerical Implementation of an Acoustic Pressure Gradient Prediction," *Journal of Sound and Vibration*, **319**, pp. 1200–1221 (2009), DOI: 10.1016/j.jsv.2008.06.028.

[46]Farassat, F. and Succi, G. P., "A Review of Propeller Discrete Frequency Noise Prediction Technology with Emphasis on Two Current Methods for Time Domain Calculations," *Journal of Sound and Vibration*, Vol. 71, (3), August 1980, pp. 399–419, DOI: 10.1016/0022-460X(80)90422-8.

[47]Farassat, F., "Derivation of formulations 1 and 1A of Farassat," NASA TM 2007-214853, Hampton, VA, 2007.

[48]Brentner, K. S. and Farassat, F., "Modeling Aerodynamically Generated Sound of Helicopter Rotors," *Progress in Aerospace Sciences*, Vol. 39, (2), February 2003, pp. 83–120, DOI: 10.1016/S0376-0421(02)00068-4.

[49]Ffowcs Williams, J. and Hawkings, D. L., "Sound Generation by Turbulence and Surfaces in Arbitrary Motion," *Philosophical Transactions of the Royal Society A: Mathematical, Physical and Engineering Sciences*, Vol. 264, (1151), May 1969, pp. 321–342, DOI: 10.1098/rsta.1969.0031.

[50]Johnson, W., *Helicopter Theory*, Princeton University Press, Princeton, NJ, 1980, p. 118.

[51]Wright, S. and Cummings, H., "Pretest Comprehensive Analysis for the Urban Air Mobility Side-by-Side Test Stand," Proceedings of the Vertical Flight Society Technical Conference on Aeromechanics Design for Transformative Vertical Flight, San Jose, CA, January 2022.

[52]Abras, J., Hariharan, N. S., and Narducci, R. P., "Wake Breakdown of High fidelity Simulations of a Rotor in Hover," Paper AIAA 2019-0593, Proceedings of the AIAA SciTech Forum, San Diego, CA, January 7–11, 2019.

[53]Abras, J., Narducci, R. P., and Hariharan, N. S., "Impact of High-Fidelity Simulation Variations on

Wake Breakdown ofa Rotor in Hover," Paper AIAA 2020-0531, Proceedings of the AIAA SciTech Forum, Orlando, FL, January 7–11, 2020.

[54]Bodling, A. and Potsdam, M., "Numerical Investigation of Secondary Vortex Structures in a Rotor Wake," *Journal of the American Helicopter Society*, **67**, 042007 (2022), DOI: 10.4050/JAHS.67.042007.

[55]Leishman, J. G., *Principles of Helicopter Aerodynamics*, Cambridge University Press, New York, NY, 2000, Chapter 5.

[56]Caprace, D. G., Diaz, P. V., and Yoon, S., "Simulation of the Rotorwash Induced by a Quadrotor Urban Air Taxi in Ground Effect," Proceedings of the 79th Anual Forum of the Vertical Flight Society, West Palm Beach, FL, May 2023.

List of Figures

1 Six-passenger side-by-side air taxi VTOL concept design rendering from NASA [34]. . . 5

2 Side-by-side rotor configuration with no overlap. 7

3 Rotor blade planform. 7

4 Near-body grids of the rotor blade: (a) blade root and (b) blade tip. 9

5 Off-body grids for the IGE cases for 0% overlap case: (a) H/D = 0.5 and (b) H/D = 1. . 11

6 Overlapping rotor geometry exhibiting the overlap area, A_{ov} 12

7 Performance comparison between IGE and OGE for the 0% and 25% overlap cases: (a) thrust coefficient and (b) torque coefficient. 13

8 Figure of merit convergence plots for the 0% and 25% overlap cases: (a) 0% overlap and (b) 25% overlap. 14

9 Iso-surfaces of the q-criterion with the vorticity magnitude for the 0% overlap case: (a) OGE, (b) $H = 1D$, and (c) $H = 0.5D$. 16

10 Iso-surfaces of the q-criterion with the vorticity magnitude for the 25% overlap case: (a) OGE, (b) $H = 1D$, and (c) $H = 0.5D$. 17

11 Comparison of λ_i (inflow ratio) between the OGE and IGE cases for the 0% overlap configuration. The black bar represents the rotor disk plane: (a) OGE, (b) $H = 1D$, and (c) $H = 0.5D$. 18

12 Comparison of λ_i (inflow ratio) between the OGE and IGE cases for the 25% overlap configuration. The black bar represents the rotor disk plane: (a) OGE, (b) $H = 1D$, and (c) $H = 0.5D$. 19

13 Hazardousness for the IGE cases of the 0% and 25% overlap configuration at $H = 0.5D$. 21

14 Hazardousness for the IGE cases of the 0% and 25% overlap configuration at $H = 1D$. . 21

15 Normal force for the 0% overlap configuration comparing the in- and out-of-ground effect cases: (a) OGE, (b) $H = 1D$, and (c) $H = 0.5D$. 22

16 Normal force for the 25% overlap configuration comparing the in- and out-of-ground effect cases: (a) OGE, (b) $H = 1D$, and (c) $H = 0.5D$. 22

17 The non-dimensional normal force coefficient for the 0% overlap at four different radial locations: (a) $r/R = 0.5$, (b) $r/R = 0.75$, (c) $r/R = 0.90$, and (d) $r/R = 1.0$. 23
18 The non-dimensional normal force coefficient for the 25% overlap at four different radial locations: (a) $r/R = 0.5$, (b) $r/R = 0.75$, (c) $r/R = 0.90$, and (d) $r/R = 1.0$. 24
19 Blade sectional thrust coefficient for the IGE cases: (a) 0% overlap at $H = 0.5D$, (b) 0% overlap at $H = 1D$, (c) 25% overlap at $H = 0.5D$, and (d) 25% overlap at $H = 1D$. . . 25
20 Comparison of $dF_z/d\Psi$ of the left rotor at the 75% span for the IGE and OGE cases of the 0% and 25% overlap configurations: (a) 0% overlap and (b) 25% overlap. 25
21 Comparison of the total acoustic pressure for IGE and OGE cases of the 0% and 25% overlap configurations: (a) 0% overlap and (b) 25% overlap. Observers are located on the ground directly below the hub center of the vehicle. 26
22 Comparison of A-weighted SPL for the IGE and OGE cases of the 0% and 25% overlap configurations: (a) 0% overlap and (b) 25% overlap. 27
23 Comparison of noise intergrand results of the left rotor for all IGE cases of the 0% and 25% overlap configurations. 28
24 Comparison of A-weighted OASPL for the IGE and OGE cases of the 0% and 25% overlap configurations: (a) 0% overlap and (b) 25% overlap. 29
25 Noise directivity (A-weighted and unweighted) for all IGE cases of the 0% and 25% overlap configuration: (a) $H = 0.5D$ and (b) $H = 1D$. 30

List of Tables

1 Basic properties for the side-by-side air taxi 6

2 Simulation settings | All overlap cases 8

3 Computational size and cost | All overlap cases 9

4 FM that is averaged over the last revolution for 0% and 25% overlap cases for the combined rotors 15